specific LIF small interfering RNA (siRNA) expressing plasmids were pSilencer-siLIF367, pSilencer-siLIF589 and pSilencer-siLIF640, respectively. The SEKI cells were transfected using Lipofectamine 2000 (Invitrogen, Carlsbad, CA) with the three kinds of pSilencer-siLIF or a negative control pSilencer (pSlilencer-siNC; Ambion Inc.) vector that expresses a hairpin siRNA with a limited homology to any known sequences in the human genome, and pGK-neomycin vector (kindly provided by Dr. Kazuhisa Sekimizu from University of Tokyo, Japan) for the selection of stably transfected cells. Stable transfected cell lines, designated SEKI-siLIF367, SEKI-siLIF589, SEKI-siLIF640 and SEKI-siNC, were established after selection in the medium containing 150 μg/ml G-418 (Gibco) for 3–4 weeks and then were maintained in the medium containing 75 μg/ml G-418.

Immunoblotting

Twenty μg of whole cell lysates as determined using a Protein Assay (Bio-Rad Laboratories, Hercules, CA) from SEKI cells and three kinds of SEKI-siLIF cells were loaded per lane for the Western blot analysis. LIF and glyceraldehyde-3-phosphate dehydrogenase (GAPDH) were detected with primary goat polyclonal antibodies (Santa Cruz Biotechnology, Santa Cruz, CA) and a donkey anti-goat secondary antibody coupled to horseradish peroxidase (Chemicon International Inc., Temecula, CA).

In vitro cell proliferation

To determine the effects of LIF expression on cell proliferation, 1×10^5 cells of parental, empty vector-transfected (mock) and LIF-reduced SEKI cells were seeded in six-well plates in 5 ml of growth medium on day 0. The cells were counted using a hemocytometer periodically until day 6.

Osteoclast formation in vitro

LIF and/or SEKI cells-induced osteoclastogenesis was examined in vitro using a co-culture system previously described by Takahashi et al. [14]. Briefly, osteoblastic stromal cells were prepared from digests of mouse calvaria, while the cells of the hematopoietic lineage were prepared from the bone marrow of mouse tibia and femora. These cells were cultured together in α-MEM containing 10% FBS with rhM-CSF (50 ng/ml, R&D system) alone or together with rhRANKL (positive control) (sRANKL; Peprotech EC, London, UK), rhLIF or SEKI cells (parental, empty vector-transfected (mock) and LIF-reduced cells) for 7 days. The cultured cells were subjected to tartrate-resistant acid phosphatase (TRAP) staining as described previously [15], and then the number of TRAP-positive multinucleated cells were counted.

In vivo bone metastasis model

Subconfluent parental, mock and LIF-reduced SEKI cells were harvested with 0.2% EDTA and 0.02% trypsin, incubated in culture medium and suspended in PBS just before cardiac inoculation (2×10^5 cells/0.1 ml PBS).

A hundred μl of these cell suspensions were injected into the left heart ventricle of the nude mice according to the procedure described previously [16]. The development of osteolytic bone metastases was monitored by radiographs. The mice were sacrificed when hind leg paralysis was noted, while the mice, in which hind leg paralysis was not seen, were observed until 8 weeks after the inoculation of tumor cells. Thereafter, the mice were sacrificed, and the number of visible tumor colonies in the skeleton was counted.

Immunohistochemistry

Immunohistochemical staining for LIF was performed on paraffin-embedded sections of the bone metastasis specimens obtained from nude mice inoculated with SEKI cells according to the previously described method [17]. Briefly, the sections (4 μm) were de-paraffinized with xylene and rehydrated through a graded series of ethanol. After the inhibition of endogenous peroxidase, the sections were incubated with a goat polyclonal anti-LIF antibody (Santa Cruz Biotechnology, CA) at 4°C overnight, followed by incubation with biotinylated link antibody and peroxidase-labeled streptavidin (Nichirei, Tokyo, Japan) at room temperature for 20 min. The sections were then reacted in 3,3′-diaminobenzidine tetrahydrochloride (DAB), and then counterstained with hematoxylin. A tissue sample from the xenograft of SEKI cells in nude mice was used as a positive control, while a section incubated with PBS instead of the primary antibody was used as a negative control.

Histomorphometry

The femoral epiphysis, in which bone destruction was detected by a radiograph and bone metastasis was histologically proven, of each mouse was subjected to a morphometric analysis. The femoral epiphysis, in which bone destruction was not evident on a radiograph and bone metastasis was not histologically proven, of each mouse was also subjected to a morphometric analysis as a control. Histological sections stained with hematoxylin and eosin were evaluated. The following parameters were determined: volume occupied by bone as a fraction of the total tissue volume [BV/TV (%)] and eroded bone surface as a fraction of the trabecular bone surface [ES/BS (%)].

Statistical analysis

The values are expressed as the mean ± SD. Significant differences between the growth curves were determined by two-way factorial ANOVA with respect to time and cell lines, followed by Turkey–Kramer test. Significant differences between the two groups were determined using the unpaired *t*-test. *P* values <0.05 were considered to be significant.

Results

Stable RNA interference of LIF in SEKI cells

To reduce the expression of LIF in SEKI cells, cells were transfected with plasmids that expressed short hairpin RNA molecules targeted to three different sites, beginning positions 367, 589 and 640 in human LIF mRNA (GenBank/EMBL/DDBJ databanks accession number NM002309). Stably transfected cell lines were established and subjected to immunoblotting to identify clonal cells with reduced expression of LIF protein (Fig. 1a). The reduced expression of LIF mRNA in the stably transfected cell lines was also confirmed by RT-PCR (data not shown). Densitometry demonstrated that LIF expression in SEKI-siLIF640 cell line (siRNA#3) was reduced to approximately 20% of that seen in the parental SEKI, and this cell line was used as the LIF-reduced cells for further experiments. To examine the effect of LIF expression upon the proliferation of SEKI cells in vitro, cell growth was quantified over a 6-day interval after incubating cells at low density in standard culture medium (Fig. 1b). The proliferation of parental, mock and LIF-reduced SEKI cells did not differ significantly, thus suggesting that expression levels of LIF did not affect cell growth under normal culture conditions.

Effect of reduced LIF-expression in SEKI cells on differentiation of osteoclasts

The differentiation of hematopoietic cells (HPCs) into osteoclasts (OCLs) did not occur when these cells were cultured with M-CSF alone, while such differentiation was observed when HPCs were cultured with M-CSF plus RANKL (positive control). To determine whether LIF and/or SEKI cells can induce the differentiation of HPCs into OCLs, different doses of LIF (0.02–20 ng/ml) and different number of SEKI cells (1×10^2–2×10^4 cells/well) were cultured with HPCs along with M-CSF for 7 days. TRAP-positive multinucleated cells were observed as was seen in the presence of RANKL (positive control), and their number increased in a dose–responsive manner (data not shown).

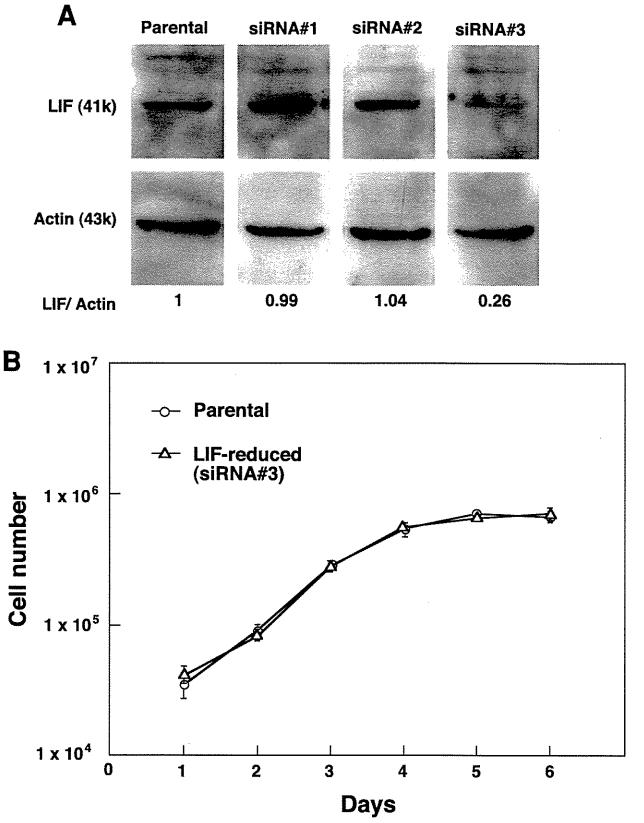

Fig. 1 Establishment of SEKI cells with reduced expression of LIF using the siRNA technique. **a** Immunoblotting for LIF protein in parental SEKI and its sub-lines. Three kinds of small interfering RNA (siRNA) specific to human LIF (#1, hLIF 367–385; #2, hLIF 589–607; #3, hLIF 640–658) were ligated into the pSilencer 2.0-U6 vector, and parental SEKI cells were transfected with these vectors and/or a negative control pSilencer vector using Lipofectamine 2000. Next, stable transfected cell lines were established. The whole cell lysates (20 μg) were prepared from the parental and three kinds of LIF-reduced SEKI cells, separated on 7.5% SDS-polyacrylamide gel electrophoresis (SDS-PAGE), and immunoblotted to detect LIF protein. An immunoblot with antibody against actin was used as a control. Relative expression levels of LIF normalized by actin levels were quantified by densitometer and shown at the bottom. **b** Proliferation curves of the parental and LIF-reduced (siRNA#3) SEKI cells. 1×10^5 of parental and LIF-reduced SEKI cells per well were seeded in six well plates in 5 ml of growth medium on day 0. Cells were counted using a hemocytometer. Data are presented as the mean (±SD) values for cell number ($n = 3$). Growth curves of these cell lines were similar, and there were no significant differences among them

The effect of the LIF expression levels in SEKI cells on the differentiation of HPCs into OCLs was next examined. The cells with a reduced expression of LIF were prepared using a siRNA technique (LIF-reduced) and the cells were transfected with empty vector (mock) from the parental SEKI cells (parental). Thereafter, the parental, mock and LIF-reduced SEKI cells (1×10^4 cells/well) were co-cultured with HPCs in the presence of M-CSF for 7 days. Figure 2 shows that the number of TRAP-positive multinucleated cells significantly decreased in the LIF-reduced

SEKI cells in comparison to those in the parental SEKI cells and mock cells ($P < 0.005$). There was no significant difference between the number of TRAP-positive multinucleated cells in the parental SEKI cells and that in the mock cells (Fig. 2).

Bone metastases after inoculation of parental, mock and LIF-reduced SEKI cells

Bone metastases were detected by radiographs in all the mice at 3–7 weeks after inoculation of parental and mock SEKI cells (Figs. 3a, 4a). Hind leg paralysis also developed in these mice. There was no significant difference between their numbers of tumor colonies (Fig. 4b). However, the period, at which hind leg paralysis was first noted, was significantly longer in the mice inoculated with the mock SEKI cells in comparison to that seen in the mice inoculated with parental SEKI cells, although its reason for this was unknown (Fig. 4c). In the mice inoculated with LIF-reduced SEKI cells, on the other hand, bone metastases were found in 5 of 13 mice at 8 weeks postinoculation (Fig. 4a). Hind leg paralysis developed in one of five these mice in which bone metastases were found. Furthermore, the number of tumor colonies decreased and the period during which bone metastases were first detected by radiographs, was prolonged in comparison to those in the mice inoculated with parental and mock SEKI cells (Fig. 4b, c). The differences between the incidence, the number of tumor colonies and the period in the mice inoculated with LIF-reduced SEKI cells and those in the mice inoculated with parental and mock SEKI cells were all statistically significant ($P < 0.001$).

A histological examination of bone metastasis specimens revealed infiltrated tumor cells in the bone marrow cavity (Fig. 3b-1). Numerous osteoclasts were accumulated around the tumor cells in the bone marrow, and resorbing the bone matrix (Fig. 3b-1, 2). Immunohistochemistry for LIF revealed the expression of LIF in the infiltrated tumor cells in the bone marrow (Fig. 3b-3).

Histomorphometry

Histomorphometric analyses confirmed the radiographic findings on bone metastases at 3 weeks after inoculation of the parental SEKI cells. A reduction in the bone volume (BV) relative to tissue volume (TV) and an increase of eroded bone surface (ES) relative to trabecular bone surface (BS) were noted at the tumor sites in comparison to those at the non-tumor sites (Fig. 5). These differences were also statistically significant ($P < 0.01$). The findings in the histomorphometry together with those in the in vitro experiment for osteoclastogenesis and the histological examination suggest that tumor cells in the bone marrow induced osteolysis through the activation of osteoclasts possibly by LIF.

LIF expression in human melanoma-derived cultured cells

To examine whether LIF expression, which is observed in SEKI cells, is a universal event to melanoma, semi-quantitative RT-PCR was performed using a human melanoma cDNA panel prepared from nine human melanoma-derived cultured cells. Figure 6 shows that LIF expression was found in seven of nine cell lines, thus suggesting that the LIF expression is a universal event in melanoma. In addition, the expression of PTHrP, which is a master regulator in the osteoclastogenesis during the bone metastasis in solid tumors, was examined in these cell lines. The expression of PTHrP, however, was found in four of nine cell lines (Fig. 6).

Discussion

Bone metastasis is a common problem in patients with various cancers. This results in bone pain, pathological fractures, neurological deficits and/or hypercalcemia. Cancer cells become distributed in bone through a hematogenous route. The process of such hematogenous spread in soft tissue metastasis include shedding of cancer cells from a primary tumor into the circulation, colonization in a target organ, extravasation into the surrounding tissue, initiation and maintenance of growth, and vascularization of the metastatic tumor. In bone metastasis, however, a further step, in which cancer cells invade and proliferate in the bone matrix, is necessary in addition to the above steps for the soft tissue metastasis. Current evidence suggests that osteoclasts play a crucial role in this step for tumor-associated osteolysis [1], and several osteoclastogenic factors, i.e. PTHrP [2, 5], IL-8 [18, 19] and/or PGE2 [20], have been implicated in the activation of osteoclastic bone resorption during tumor-associated osteolysis in solid tumors. Melanoma, on the other hand, frequently metastasizes to the bone, however, its pathophysiology is still poorly understood.

The present study demonstrated that cardiac inoculation of LIF-producing melanoma-derived cultured cells (SEKI) resulted in the development of multiple osteolytic lesions within 4 weeks postinoculation with a success rate of 100%. LIF was first identified as a factor which induced macrophage differentiation from M1 murine myeloid leukemia cells and suppressed their proliferation in vitro [10]. Subsequently, LIF has been shown to induce osteoclast formation by increasing the expression of RANKL in osteoblasts [13]. RANKL binds to the RANK on osteoclast

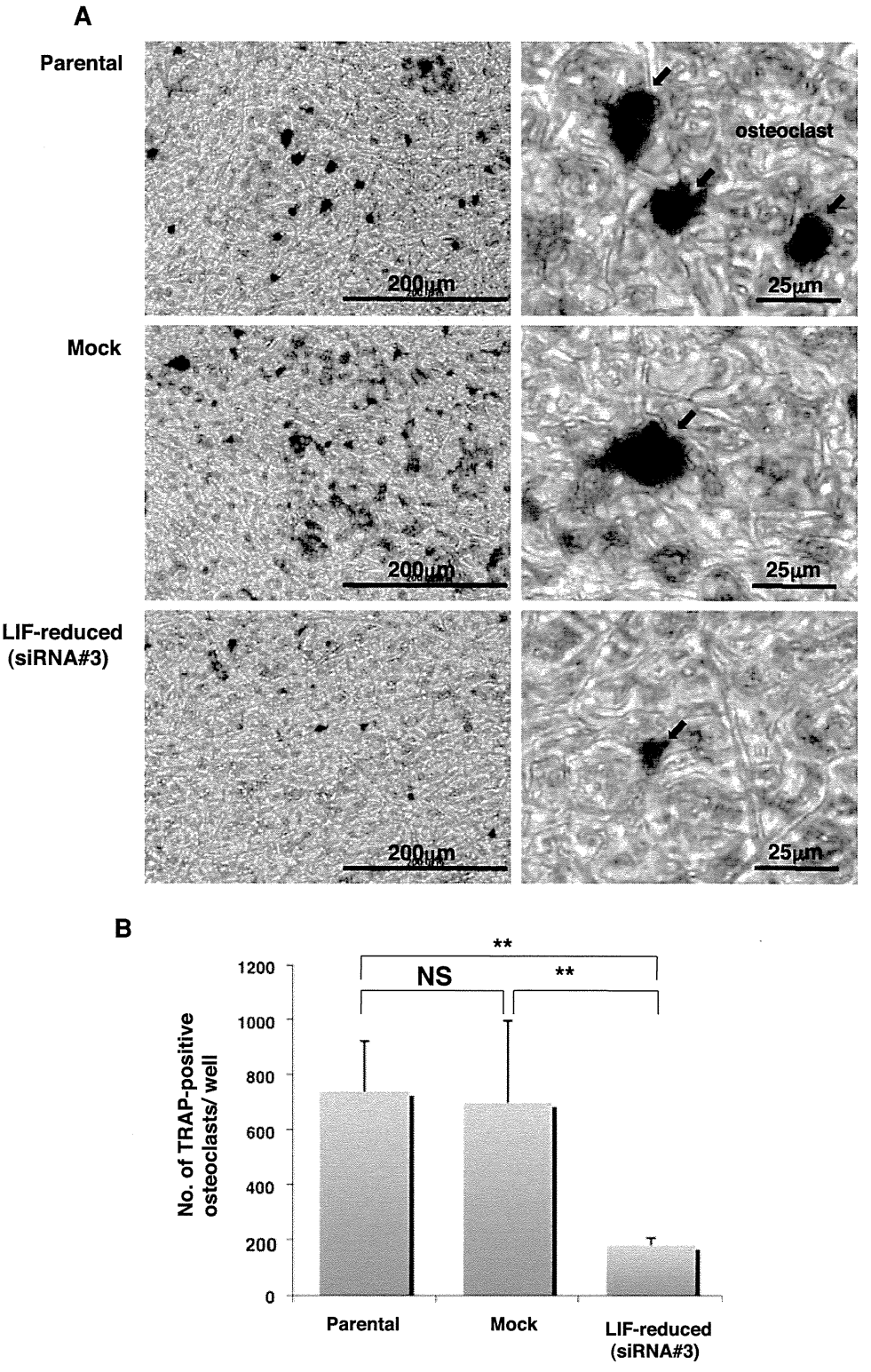

Fig. 2 Osteoclast formation in vitro. **a** Osteoclast development from mouse bone marrow cells, cultured with parental, mock and LIF-reduced (siRNA#3 in Fig. 1) SEKI cells (1×10^4 cells/well), was determined by TRAP staining. Lower magnification (*left*) and higher magnification (*right*). **b** The number of TRAP-positive multinucleated cells significantly decreased when the cells were cultured with LIF-reduced SEKI cells in comparison to those when cultured with parental and/or mock SEKI cells ($n = 5$; NS, not significant; ** $P < 0.005$)

precursors, which thus induces the formation of activated osteoclasts. The present study demonstrated that LIF and/or LIF-producing SEKI cells, in fact, induced the formation of activated osteoclasts in vitro. The effect of LIF expression on osteoclast formation and bone metastases of SEKI cells was further examined using a siRNA technique. The reduction of the LIF expression in SEKI cells was associated with a reduction of the osteoclastogenic activity of SEKI cells in vitro. Furthermore, a reduction of the LIF expression in SEKI cells was also associated with a reduction in the incidence and number of tumor colonies of bone metastases, and/or a prolongation of the period during

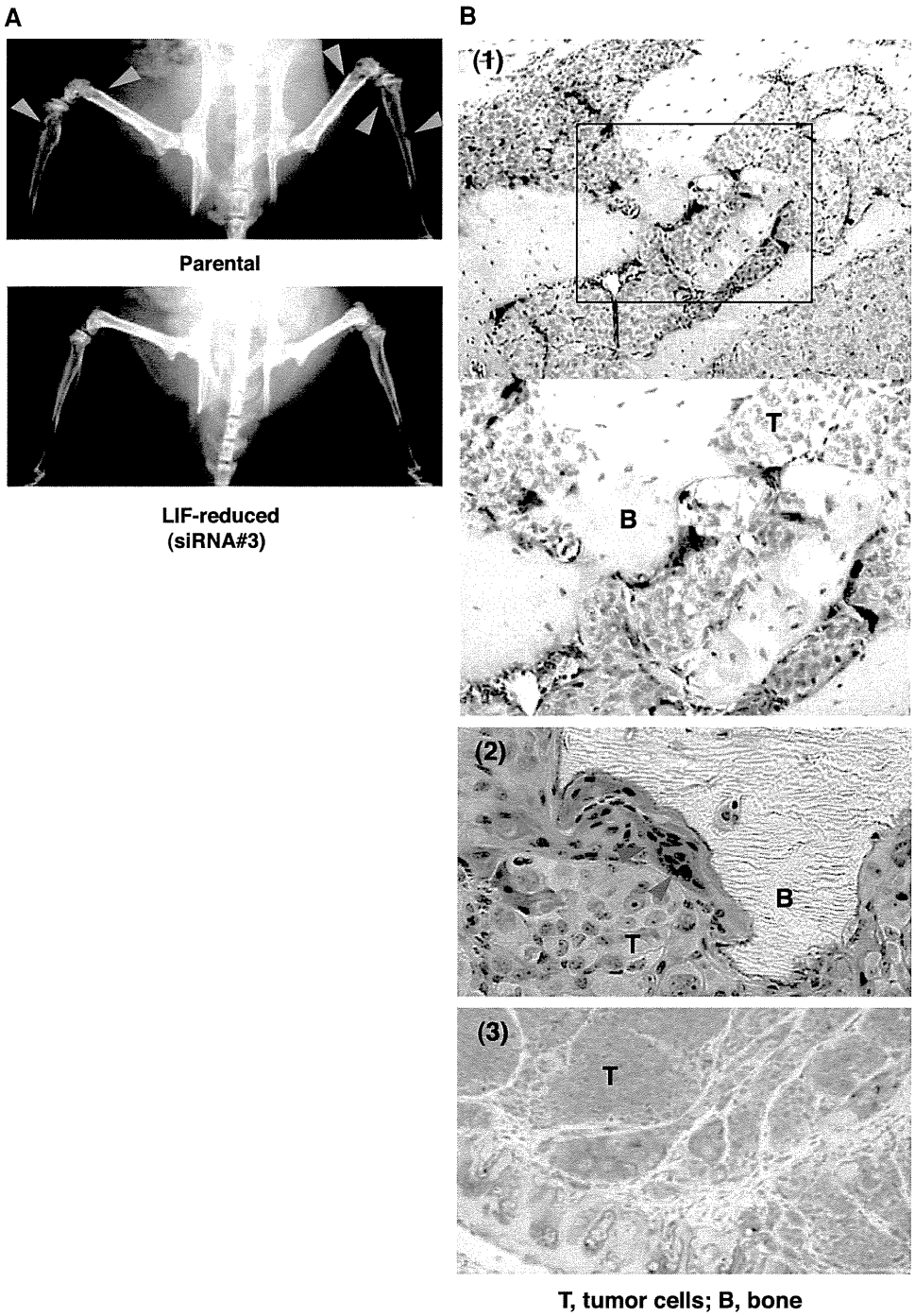

Fig. 3 Radiological and histological findings of SEKI cells-induced bone metastases in nude mice. **a** Representative radiographs of the hind limbs from mice 4 weeks after the inoculation of parental and LIF-reduced SEKI cells. Multiple osteolytic lesions (*arrow head*) were found in the mice inoculated with parental SEKI cells, while no osteolytic lesions were found in the mice inoculated with LIF-reduced SEKI cells. **b** Histological views of SEKI cells-induced bone metastasis in nude mice. (1) TRAP staining: The bone marrow cavity is almost completely replaced by the infiltrated tumor cells, and the volume of the trabecular bone is diminished. Numerous TRAP-positive cells (bone-resorbing osteoclasts) are seen on the endosteal bone surface. Lower magnification (*top*) and higher magnification (*bottom*). (2) Osteoclastic bone resorption (H&E staining; arrow head, osteoclast). (3) Immunostaining of LIF: Infiltrated tumor cells into the bone marrow cavity are positively stained with LIF

which bone metastases were first detected in vivo. These findings suggest that LIF is a major mediator in the SEKI cell-induced osteolysis in terms of the activation of osteoclastic bone resorption. Is this molecular mechanism implicated in the bone metastasis of melanoma? To answer this question, the expression of LIF was examined in nine human melanoma-derived cultured cells. The expression of LIF was found in seven of nine cell lines, whereas the expression of PTHrP, which is one of the master regulators in tumor-associated osteolysis in various cancers [2, 5], was noted in only four of nine cell lines. This is consistent with the previous data described by Mattei et al. [21], which showed expression of LIF in melanoma-derived cell lines. LIF might play a crucial role in melanoma-induced osteolysis. Sanchez-Sweatman et al. [22] reported that tumor cells directly degrade bone matrix through tumor-derived MMPs. They also found a reduction of osteoclast number in the resorption pits of the bone in this model. The present study, however, showed an increased number of osteoclasts on the bone surface at the metastatic site in the

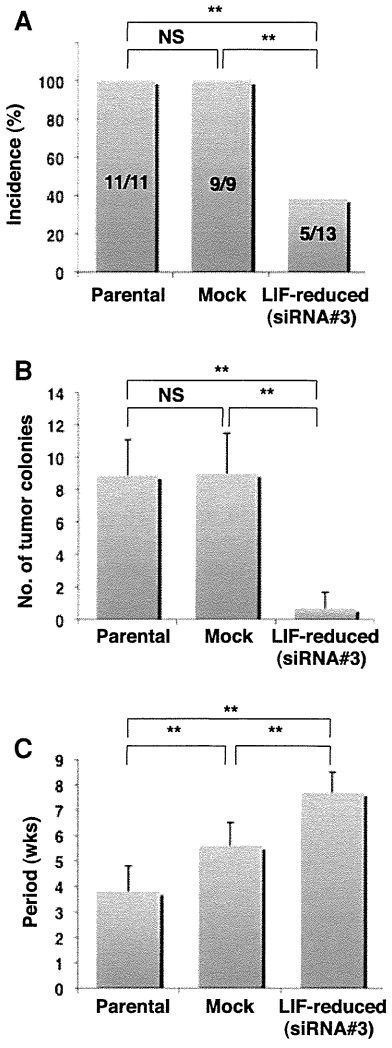

Fig. 4 Bone metastases in mice after the inoculation of parental ($n = 11$), mock ($n = 9$) and LIF-reduced (siRNA#3 in Fig. 1; $n = 13$) SEKI cells. **a** The incidence (%) of bone metastases in the mice inoculated with parental, mock and LIF-reduced (siRNA#3) SEKI cells. The numbers of mice examined and those presenting bone metastases after inoculation of the cells are shown as a denominator and a numerator, in the bars, respectively. NS, not significant; $^{**}P < 0.001$. **b** The number of tumor colonies in the mice inoculated with parental, mock and LIF-reduced (siRNA#3) SEKI cells. The mice were sacrificed when hind leg paralysis was noted, and visible tumor colonies of bone metastases were counted at autopsy. Values represent the mean ± SD. NS, not significant; ** $P < 0.001$. **c** The periods (weeks) from the inoculation of the cells to the first detection of bone metastases on radiographs are shown. Bone metastasis was monitored weekly by radiographs, and mice without bone metastasis were observed until 8 weeks postinoculation. When hind leg paralysis was noted prior to the detection of bone metastases on radiographs, it was considered to be the first detection of bone metastases since it is hard to detect the bone metastases to the vertebral bone on radiographs. Values represent the mean ± SD. ** $P < 0.001$

TRAP-staining of the histological sections. Furthermore, the reduced expression of LIF in parental SEKI cells, which decreased the number of activated osteoclast in vitro, thus resulted in the suppression of bone metastases in vivo. These findings indicate that osteoclasts, which are activated by tumor cell-derived LIF, thus play an important role in the bone destruction of SEKI cell-induced osteolysis.

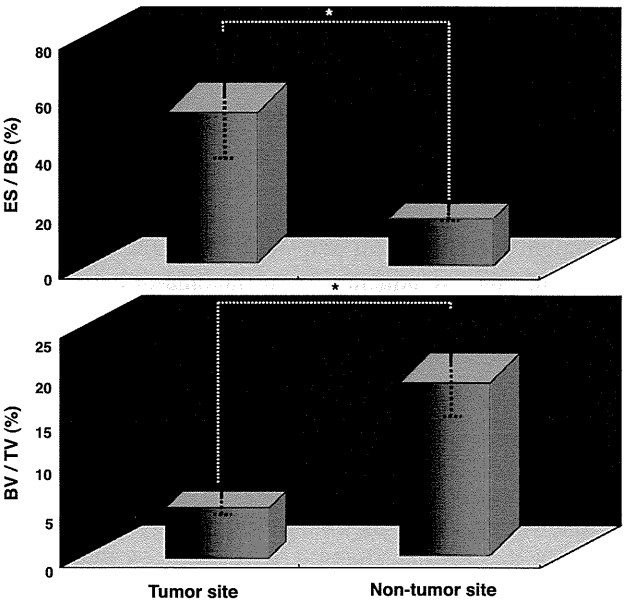

Fig. 5 A histomorphometric analysis in a bone metastasis model of human melanoma derived cultured cells (SEKI). Longitudinal sections of the femoral epiphysis were analyzed to determine BV/TV (%) and ES/BS (%) in the tumor site and non-tumor site as a control. Data represent the means ± SD in each of the sites ($n = 5$). BV, bone volume; TV, tumor volume; ES, eroded surface; BS, bone surface.*significant difference ($P < 0.01$)

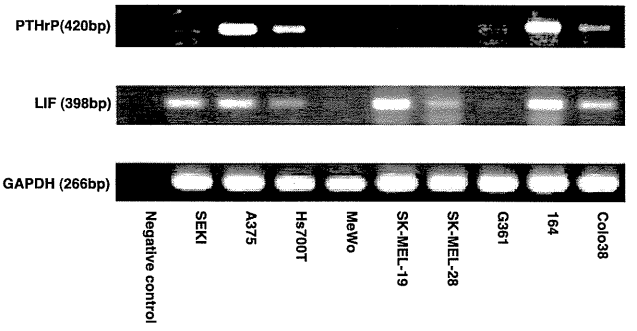

Fig. 6 LIF and PTHrP expression in human melanoma-derived cultured cells. Total RNAs were extracted from the cells and subjected to RT-PCR with primer pairs specific for LIF, PTHrP and GAPDH (as an internal control). Mock is the PCR product amplified from the SEKI cDNA (-RT). LIF is expressed in seven of nine melanoma-derived cells, while PTHrP is expressed in four of nine cell lines

The process of bone metastasis is unique, in terms of the crucial role of osteoclasts. Cancer cells, which are arrested in the bone marrow space, could stimulate osteoclastogenesis through soluble factors, which stimulate bone destruction. A better understanding of the molecular mechanism in this step may provide us with important

insight into the development of more effective therapies for bone metastasis. Recently, Wysoczynski et al. [23] demonstrated that LIF, which is produced in the bone marrow, act as a chemotactic factor to the bone in the bone metastasis of rhabdomyosarcoma cells, suggesting another role of LIF in the process of bone metastasis. This findings together with our present data described here suggest that LIF might therefore be a potentially effective therapeutic target in the treatment of melanoma-induced bone metastasis.

References

1. Roodman GD (2004) Mechanisms of bone metastasis. N Engl J Med 350:1655–1664. doi:10.1056/NEJMra030831
2. Iguchi H, Tanaka S, Ozawa Y et al (1996) An experimental model of bone metastasis by human lung cancer cells: the role of parathyroid hormone-related protein in bone metastasis. Cancer Res 56:4040–4043
3. Croucher PI, Shipman CM, Lippitt J et al (2001) Osteoprotegerin inhibits the development of osteolytic bone disease in multiple myeloma. Blood 98:3534–3540. doi:10.1182/blood.V98.13.3534
4. Abe M, Hiura K, Wilde J et al (2002) Role for macrophage inflammatory protein (MIP)-1alpha and MIP-1beta in the development of osteolytic lesions in multiple myeloma. Blood 100:2195–2202
5. Guise TA, Yin JJ, Taylor SD et al (1996) Evidence for a causal role of parathyroid hormone-related protein in the pathogenesis of human breast cancer-mediated osteolysis. J Clin Invest 98:1544–1549. doi:10.1172/JCI118947
6. Onuma E, Sato K, Saito H et al (2004) Generation of a humanized monoclonal antibody against human parathyroid hormone-related protein and its efficacy against humoral hypercalcemia of malignancy. Anticancer Res 24:2665–2673
7. Shimoyama M (1975) SEKI strain. In: Oboshi S, Sugano H (eds) In vitro culture of human cancer cells. Asakura Shoten, Tokyo, pp 208–215
8. Kondo Y, Sato K, Ueyama Y et al (1981) Serum sialyltransferase and liver catalase activity in cachectic nude mice bearing a human malignant melanoma. Cancer Res 41:2912–2916
9. Mori M, Yamaguchi K, Honda S et al (1991) Cancer cachexia syndrome developed in nude mice bearing melanoma cells producing leukemia-inhibitory factor. Cancer Res 51:6656–6659
10. Gearing DP, Gough NM, King JA et al (1987) Molecular cloning and expression of cDNA encoding a murine myeloid leukaemia inhibitory factor (LIF). EMBO J 6:3995–4002
11. Kurzrock R, Estrov Z, Wetzler M et al (1991) LIF: not just a leukemia inhibitory factor. Endocr Rev 12:208–217
12. Alexander HR, Billingsley KG, Block MI et al (1994) D-factor/leukaemia inhibitory factor: evidence for its role as a mediator in acute and chronic inflammatory disease. Cytokine 6:589–596. doi:10.1016/1043-4666(94)90045-0
13. Palmqvist P, Persson E, Conaway HH et al (2002) IL-6, leukemia inhibitory factor, and oncostatin M stimulate bone resorption and regulate the expression of receptor activator of NF-kappa B ligand, osteoprotegerin, and receptor activator of NF-kappa B in mouse calvariae. J Immunol 169:3353–3362
14. Takahashi N, Akatsu T, Udagawa N et al (1988) Osteoblastic cells are involved in osteoclast formation. Endocrinology 123:2600–2602
15. van de Wijngaert FP, Burger EH (1986) Demonstration of tartrate-resistant acid phosphatase in un-decalcified, glycolmethacrylate-embedded mouse bone: a possible marker for (pre)osteoclast identification. J Histochem Cytochem 34:1317–1323
16. Arguello F, Furlanetto RW, Baggs RB et al (1992) Incidence and distribution of experimental metastases in mutant mice with defective organ microenvironments (genotypes Sl/Sld and W/Wv). Cancer Res 52:2304–2309
17. Oda Y, Takahira T, Kawaguchi K et al (2003) Altered expression of cell cycle regulators in myxofibrosarcoma, with special emphasis on their prognostic implications. Hum Pathol 34:1035–1042. doi:10.1053/S0046-8177(03)00404-0
18. Bendre MS, Gaddy-Kurten D, Mon-Foote T et al (2002) Expression of interleukin 8 and not parathyroid hormone-related protein by human breast cancer cells correlates with bone metastasis in vivo. Cancer Res 62:5571–5579
19. Bendre MS, Margulies AG, Walser B et al (2005) Tumor-derived interleukin-8 stimulates osteolysis independent of the receptor activator of nuclear factor-kappaB ligand pathway. Cancer Res 65:11001–11009. doi:10.1158/0008-5472.CAN-05-2630
20. Ono K, Akatsu T, Murakami T et al (2002) Involvement of cyclo-oxygenase-2 in osteoclast formation and bone destruction in bone metastasis of mammary carcinoma cell lines. J Bone Miner Res 17:774–781. doi:10.1359/jbmr.2002.17.5.774
21. Mattei S, Colombo MP, Melani C et al (1994) Expression of cytokine/growth factors and their receptors in human melanoma and melanocytes. Int J Cancer 56:853–857. doi:10.1002/ijc.2910560617
22. Sanchez-Sweatman OH, Lee J, Orr FW et al (1997) Direct osteolysis induced by metastatic murine melanoma cells: role of matrix metalloproteinases. Eur J Cancer 33:918–925. doi:10.1016/S0959-8049(97)00513-3
23. Wysoczynski M, Miekus K, Jankowski K et al (2007) Leukemia inhibitory factor: a newly identified metastatic factor in rhabdomyosarcomas. Cancer Res 67:2131–2140. doi:10.1158/0008-5472.CAN-06-1021

INTERNAL MEDICINE

□ CASE REPORT □

Primitive Neuroectodermal Tumor of the Pancreas

Hirokazu Doi[1], Soichi Ichikawa[1], Atsushi Hiraoka[1], Misa Ichiryu[1], Hiromasa Nakahara[1], Hironori Ochi[1], Atsushi Tanabe[1], Akihiro Kodama[1], Aki Hasebe[1], Yasunao Miyamoto[1], Tomoyuki Ninomiya[1], Norio Horiike[1], Kazuhito Takamura[2], Hideki Kawasaki[2], Chieko Kameoka[3], Miki Kan[3], Shigekazu Doi[3], Yoshiko Soga[3], Hiromi Tamura[3], Toshiharu Maeda[3], Akinori Asaki[4], Seijin Seno[4], Haruo Iguchi[4] and Tadashi Hasegawa[5]

Abstract

The primitive neuroectodermal tumor (PNET) of the pancreas, a member of Ewing's sarcoma family of tumors, is extremely rare. We treated a 37-year-old Japanese man who had a solitary pancreatic tumor 40 mm in diameter and multiple hepatic tumors with surgical resection. The PNET was positive for CD99 on immunohistochemical staining. Fluorescence in situ hybridization (FISH) was also performed, which revealed a Ewing sarcoma breakpoint region 1 (*EWSR1*) 22q12 rearrangement. According to the Japan-Ewing protocol, chemotherapy with Ifomide (ifosfamide), etoposide, vincristine, and cyclophosphamide was given after surgery. To the best of our knowledge, to date 13 PNET cases have been reported with a mean age for all patients of 19.3 years old. Surgical resection was performed in most cases and some patients received postoperative chemotherapy. The clinicopathologic characteristics and management of this extremely rare disease are also discussed.

Key words: primitive neuroectodermal tumor, pancreas, FDG-PET

(Inter Med 48: 329-333, 2009)
(DOI: 10.2169/internalmedicine.48.1484)

Introduction

Primitive neuroectodermal tumors (PNETs) are small round cell tumors arising from soft tissue that belong to Ewing's sarcoma family of tumors (ESFT) (1). We treated an extremely rare case of PNET of the pancreas and metastasis. To the best of our knowledge, this is the only report of a case of PNET of the pancreas examined with fluorodeoxyglucose-positron emission tomography integrated with CT scanning (FDG-PET CT). Herein, we compare our findings to those of previously reported cases with respect to clinical presentation, pathologic features, therapy, and clinical outcome.

Case Report

A 37-year-old Japanese man with jaundice was admitted to Ehime Prefectural Central Hospital in August 2007, after which a pancreas tumor with a maximum size of 42 mm and multiple hepatic tumors with a maximum size of 36 mm in the 3rd, 4th, and 7th segments were shown in an abdominal ultrasonography (US) examination. Laboratory studies revealed total bilirubin at 10.1 mg/dL, direct bilirubin at 7.4 mg/dL, aspartate aminotransferase at 151 IU/L, alanine aminotransferase at 476 IU/L, alkaline phosphatase at 803 IU/L, lactate dehydrogenase at 291 IU/L, and γ-glutamyltranspeptidase at 1,683 IU/L, while amylase was within the range of normal. Tumor markers, including carcinoembryonic antigen, carbohydrate antigen 19-9, s-pancreas-

[1]Department of Gastroenterology, Ehime Prefectural Central Hospital, Matsuyama, [2]Department of Surgery, Ehime Prefectural Central Hospital, Matsuyama, [3]Department of Medical Laboratory, Ehime Prefectural Central Hospital, Matsuyama, [4]Department of Gastroenterology, National Hospital Organization Shikoku Cancer Center, Matsuyama and [5]Department of Surgical Pathology, Sapporo Medical University School of Medicine, Sapporo
Received for publication July 7, 2008; Accepted for publication October 21, 2008
Correspondence to Dr. Soichi Ichikawa, hirokazud@me.pikara.ne.jp

Table 1. Laboratory Data on Admission

WBC	7020 /μL	Blood urea nitrogen	15.0 mg/dL
RBC	475 ×10⁴ /μL	Creatinine	1.16 mg/dL
Hb	14.4 g/dL	Sodium	134 mEq/L
Hematocrit	43.1 %	Potassium	4.0 mEq/L
MCV	90.7 fl	Chloride	101 mEq/L
MCH	30.3 pg	Glucose	106 mg/dL
MCHC	33.4 %		
Platelet	18.1 ×10⁴ /μL	Prothrombin time	97.2%
		Activated partial thromboplastin time	27.4 sec
Total-bilirubin	10.1 mg/dL		
Direct-bilirubin	7.4 mg/dL	HBs-Ag	(-)
Aspartate aminotransferase	151 IU/L	Anti-HCV	(-)
Alanine aminotransferase	476 IU/L	HCV-RNA	(-)
Alkaline phosphatase	803 IU/L		
Lactate dehydrogenase	291 IU/L	CEA	1.6 ng/mL
γ-Glutamyltranspeptidase	1683 IU/L	CA19-9	41.2 U/mL
Amylase	94 IU/L	SPAN-1	131.1 U/mL
Total protein	7.2 g/dL	DUPAN-2	272 U/mL
Albumin	4.7 g/dL		

MCV, mean corpuscular volume; MCH, mean corpuscular hemoglobin; MCHC, mean corpuscular hemoglobin concentration; HBs-Ag, hepatitis B virus surface antigen; Anti-HCV, hepatitis C virus antibody; CEA, Carcinoembryonic antigen; CA19-9, Carbohydrate antigen 19-9; SPAN-1, S-pancreas-1 antigen; DUPAN-2, Pancreatic cancer associated antigen-2

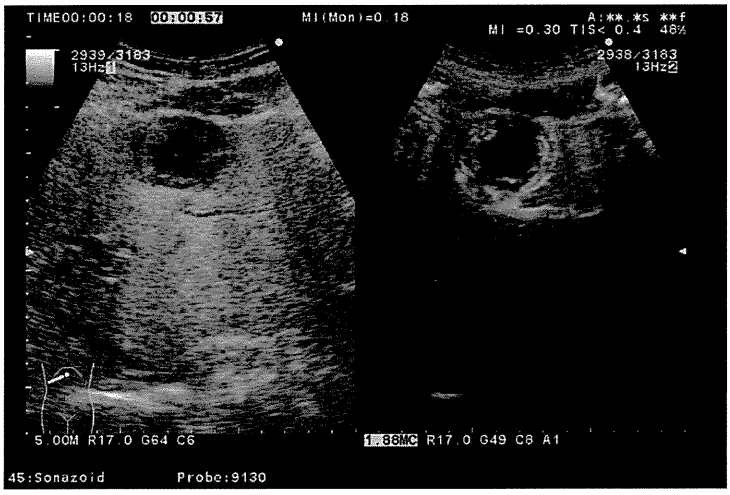

Figure 1. Abdominal ultrasonography (US) examination of a 37-year-old male showing a hepatic tumor with a maximum size of 36 mm in the 3rd segment (S3) of the left lobe of the liver. Contrast enhanced US with perflubutane (Sonazoid) showed a hepatic tumor with slight ring enhancement in the artery phase.

1 antigen, and pancreatic cancer associated antigen-2, were significantly abnormal (Table 1). Contrast-enhanced US with perflubutane (Sonazoid) (1) revealed a hepatic tumor in the left lobe with slight ring enhancement in the artery phase and a clear defect in the Kupffer phase (Fig. 1).

Endoscopic retrograde cholangiopancreatography (ERCP) revealed narrowing of the main pancreatic duct (MPD) of the head and localized severe narrowing of the distal common bile duct (CBD) with dilatation of the proximal bile ducts. Chest and abdominal computed tomography (CT) images showed a large soft tissue mass in the pancreas, along with multiple hepatic and lung metastatic lesions. The pancreas tumor and liver tumors were revealed as hypovascular by enhanced CT (Fig. 2a). Using fluorodeoxyglucose-positron emission tomography integrated with CT imaging (FDG-PET CT), the pancreas tumor and multiple hepatic and lung metastatic lesions were found to have low levels of standardized uptake value (SUV) for FDG (SUVmax =3.0) (Fig. 2b). Furthermore, magnetic resonance imaging (MRI) showed the tumors to be slightly hyperintense on T2-W images and multiple bone metastases were detected.

An ultrasound-guided percutaneous liver biopsy (USGLB) was performed for the left lobe of the liver. Based on histological findings, a metastatic carcinoma or poorly differentiated endocrine carcinoma was suspected. We performed cytoreductive surgery via a pancreatoduodenectomy and a he-

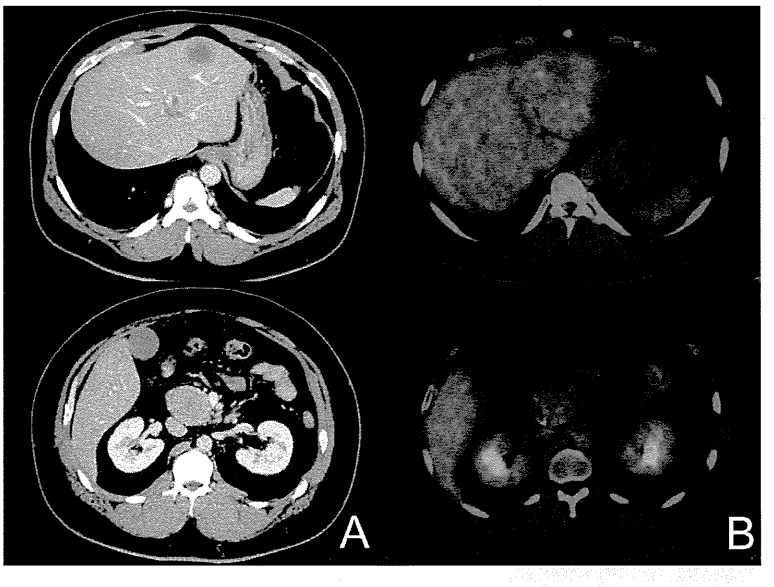

Figure 2. **A: Enhanced computed tomography (CT) showing hypovascular tumors in the pancreas and liver. B: The pancreas and hepatic tumors showed low levels of standardized uptake value (SUV) for FDG (SUVmax=3.0) in fluorodeoxyglucose-positron emission tomography integrated with CT imaging (FDG-PET CT).**

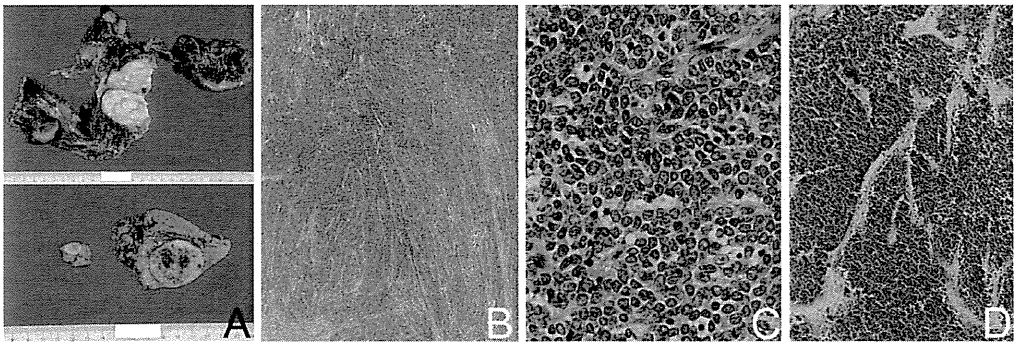

Figure 3. **A: Gross appearance of the pancreas and hepatic tumors. The cut surface of the tumors was firm, white, and fleshly. B: The tumors were composed of atypical small round cells with scant cytoplasm (Hematoxylin and Eosin staining, ×100). C: Higher magnification showing that each tumor cell had a round nucleus with a distinct nuclear membrane (Hematoxylin and Eosin staining, ×400). D: Tumor cells showing strong cytoplasmic membrane positivity to MIC2 glycoprotein (×100).**

patic resection in September 2007.

The resected specimen revealed a pancreas tumor measuring 60 mm, and hepatic tumors in the 3rd and 4th segments that measured 35 and 13 mm, respectively. A histological study showed that the pancreas tumor was composed of atypical small round cells with scant cytoplasm and each had a round nucleus with a distinct nuclear membrane. One lymph node was positive. Immunohistochemistry findings were positive for vimentin, CD99 (MIC2), CD56 and neuron-specific enolase (NSE), while they were negative for pan-cytokeratin, desmin, leucocyte common antigen (LCA), and S-100 (Fig. 3). In addition, a Ewing sarcoma breakpoint region 1 (*EWSR1*) 22q12 rearrangement was proven by a 2-color fluorescence in situ hybridization (FISH) assay (Fig. 4). Finally, we diagnosed the tumor as a primitive neuroectodermal tumor (PNET) of the pancreas.

The patient received seven cycles chemotherapy [VDC consisting of vincristine at 1.5 mg/m^2, adriamycin at 37.5 mg/m^2, cyclophosphamide at 1.2 mg/m^2, and IE consisting of Ifomide (ifosfamide) at 1.8 mg/m^2, etoposide at 100 mg/m^2] and radiation therapy for the ilium and the right tibia (total 50 Gy) following resection. One year after diagnosis, the lung and bone tumors had diminished. However, as one hepatic metastatic lesion of the 8th segment was found by FDG-PET CT, he underwent radio frequent ablation in July 2008. At the time of this writing he is in good health.

Discussion

PNET belongs to Ewing's sarcoma family of tumors

(ESFT), which are small round cell tumors that arise from primitive neuroepithelial stem cells and show morphologic, histologic, immunohistochemical, and ultrastructural evidence of neuroectodermal differentiation (2). ESFT have typical chromosomal translocations with subsequent functional fusion of the EWS gene with the transcription factor gene to form chimeric protein. The tumor cells express MIC-2 gene products (cell surface glycoprotein p30/32^{MIC2}, or CD99) and demonstrate chromosomal translocation (3). Although immunochemical staining for MIC2 is highly sensitive for ESFT (95-100%) (4), some other round cell tumors, including malignant lymphoma and rhabdomyosarcoma, show membranous immunoreactivity for MIC2 (5). ESFT show typical chromosomal translocations involving the *EWSR1* gene on 22q12. The most common translocation t(11;22)(q24;q12), resulting in the fusion product *EWS-FLI1*, occurs with an incidence of 90% (6-8). EWS is an RNA-binding protein. FLI1 is a DNA-binding transcription factor, belonging to a family of genes containing an erythroblastosis virus transforming sequence domain (9). The interphase FISH method using *EWSR1* dual color breakapart probes is sensitive and specific for the detection of rearrangement of EWS gene on chromosome 22q12, although the probes specifically identify t(22q12) but cannot specifically identify the translocation partners (10). In the present case, FISH studies showed a separated signal pattern of one green and one red, demonstrating a rearrangement of the EWS gene, and we diagnosed the pancreas tumor as a PNET of the pancreas.

Figure 4. Two-color fluorescence in situ hybridization (FISH) assay results. The probes were localized to the breakpoints on chromosome 22q12 and provided evidence of the t(22q12) translocation by showing one red and one green signal pattern on the derivative chromosome 22.

Endocrine tumor of the pancreas is also a relatively rare tumor type but it is much more common than PNET of the pancreas. And MIC2 expression is seen in normal islet cells and in up to one-third of endocrine tumors of the pancreas (4). However, endocrine tumors of the pancreas primarily occur in the adult population, with a mean age of 58 years, although rare cases have been reported in the pediatric population (11). In addition, the cells of endocrine neoplasms of the pancreas commonly display finely granular and evenly dispersed nuclear chromatin and lack nuclear molding, features not seen in PNET of the pancreas. These features, along with the lack of *EWS-FLI* fusion gene, can be used to distinguish endocrine neoplasms of the pancreas from PNET of the pancreas.

Gyorke et al reported that FDG-PET is a valuable method for diagnosis of ESFT and PNET (12). Although the intensity of uptake of FDG is thought to be lower (mean SUV 4.54+/-2.79), PET is considered to be superior to bone scintigraphy for the detection of bone metastasis associated with

Table 2. Summary of Clinical Features of Reported Cases of Primitive Neuroectodermal Tumor of the Pancreas*

Case No.	Age/Sex* [ref.]	Presenting symptoms	Tumor origin**	Tumor size (cm)	Treatment	Outcome**
1	6/W [2]	Paleness, tiredness	Pancreas head	5.4	Resection with colon segmentectomy	Alive/ 6 month
2	13/W [13]	Dyspepsia	Pancreas body/tail	22	Resection, chemotherapy	NA
3	31/M [13]	Abdominal pain	Pancreas body	NA	Chemotherapy, resection	NA
4	17/M [14]	Jaundice, abdominal pain	NA	9.0	Resection	Alive/ 33 month
5	20/M [14]	Jaundice, abdominal pain	NA	3.5	Resection	Alive/ 27 month
6	25/W [14]	Abdominal pain	NA	NA	Biopsy	NA
7	21/W [14]	Abdominal pain	NA	NA	Resection	DEAD/ postoperative complication
8	25/W [14]	Jaundice, abdominal pain	NA	8.0	Biopsy	NA
9	13/M [14]	Abdominal pain	NA	6.0	Biopsy	Alive/ 43 month
10	6/M [14]	Jaundice, abdominal pain	NA	3.5	Resection	Dead/ 48 month
11	31/M [15]	Tiredness, fever	Pancreas head/body	12	Resection, chemotherapy	Alive/ 50 month
12	33/M [16]	Abdominal pain	Pancreas body	18	Resection, chemotherapy	Alive/ 1 year
13	10/W [17]	Abdominal pain	Pancreas body/tail	10	Resection	Dead/ 3 months
14 (present case)	37/M	Jaundice	Pancreas head	6	Resection, chemotherapy	Alive/ 6 months

M, man; W, Woman. **NA, not available.

ESFT. Furthermore, detection sensitivity for small lesions (mainly represented by pulmonary metastasis) by PET is lower than that of helical CT. In the present case, the pancreas tumor and liver metastasis had a low SUV for FDG (SUVmax =3.0), while lung metastasis was shown only by helical CT and not by PET-CT. The usefulness of FDG-PET CT for PNET has not been proven and an accumulation of cases is needed.

PNET of the pancreas is extremely rare, with only 13 known cases reported (Table 2) (2, 13-17). Most of those were children or young adults (mean age, 19.3 years old), and though the major complaint associated with the disease is abdominal pain (71%), there are no characteristic symptoms. No therapeutic strategy for PNET of the pancreas has been established, because of the small number of patients. Surgical resection was performed in 11 (79%) of the reported cases and chemotherapy in 5 (36%).

When a PNET is diagnosed, the standard treatment is a multimodal therapeutic regimen, including chemotherapy, radiotherapy, and surgery. Paulussen et al reported that the 10-year disease-free survival rate of patients with a localized ESFT was about 50% (18). However, those with metastatic tumors have a much worse outcome, with a 3-year disease-free survival rate of 25% reported (19). New American-European collaborative trials such as EURO-EWING-INTERGROUP-EE99 are in progress with the goal of further improvement of the cure rate for localized and metastatic ESFT. In Japan, the Japan Ewing Sarcoma Study Group (JESS) phase II clinical trial for localized ESFT and other clinical trials that include new drugs are ongoing. The number of cases of pancreatic PNET is small, however, the establishment of therapeutic methods for PNET is expected in the near future.

In conclusion, PNET of the pancreas is an extremely rare disease and most of the affected patients have been children or young adults. To the best of our knowledge, the present case is the 14th reported case. Although uncommon, a PNET must be considered in the differential diagnosis for atypical pancreatic tumors in young patients. Establishment of therapeutic methods for PNET is expected in the near future, though accumulation of case reports is needed to establish effective diagnostic methods and treatments.

References

1. Watanabe R, Matsumura M, Chen CJ, et al. Characterization of tumor imaging with microbubble-based ultrasound contrast agent, sonazoid, in rabbit liver. Biol Pharm Bull **28**: 972-977, 2005.
2. Bulchmann G, Schuster T, Haas RJ, et al. Primitive neuroectodermal tumor of the pancreas. An extremely rare tumor. Case report and review of the literature. Klin Padiatr **212**: 185-188, 2000.
3. de Alava E, Gerald WL. Molecular biology of the Ewing's sarcoma/ primitive neuroectodermal tumor family. J Clin Oncol **18**: 204-213, 2000.
4. Weidner N, Tjoe J. Immunohistochemical profile of monoclonal antibody O13: antibody that recognizes glycoprotein p30/32^{MIC2} and is useful in diagnosis Ewing's sarcoma and peripheral neuroepithelioma. Am J Surg Pathol **18**: 486-494, 1994.
5. Enzinger FM, Weiss SW. Primitive neuroectodermal tumors and related lesions. In: Soft Tissue Tumors. 4th ed. Enzinger FM, Weiss SW, Eds. Mosby, St Louis, 2001: 1265-1321.
6. Urano F, Umezawa A, Hong W, et al. A novel chimera gene between EWS and E1A-F, encoding the adenovirus E1A enhancer-binding protein, in extraosseous Ewing's sarcoma. Biochem Biophys Res Commun **219**: 608-612, 1996.
7. Turc-Carsel C, Aurias A, Mugneret F, et al. Chromosomes in Ewing's sarcoma. I An evaluation of 85 cases and remarkable consistency of t(11;22)(q24;q12). Cancer Genet Cytogenet **32**: 229-238, 1988.
8. Landanyi A, Bridge JA. Contribution of moleculargenetic data to the classification of sarcomas. Hum Pathol **31**: 532-538, 2000.
9. Remani P, Rampling D, Link M. Immunohistochemical study of 12E7 in small round-cell tumors of the childhood: an assessment of its sensitivity and specificity. Histopathology **23**: 557-561, 1993.
10. Yamaguchi U, Hasegawa T, Morimoto Y, et al. A practical approach to the clinical diagnosis of Ewing's sarcoma/primitive neuroectodermal tumour and other small round cell tumours sharing EWS rearrangement using new fluorescence in situ hybridisation probes for EWSR1 on formalin fixed, paraffin wax embedded tissue. J Clin Pathol **58**: 1051-1056, 2005.
11. Heitz PU, Kasper M, Polak JM, et al. Pancreatic endocrine tumors. Hum Patol **13**: 263-271, 1982.
12. Gyorke T, Zajic T, Lange A, et al. Impact of FDG PET for staging of Ewing sarcomas and primitive neuroectodermal tumors. Nucl Med Commun **27**: 17-24, 2006.
13. Luttges J, Pierre E, Zamboni G, et al. Malignant non-epithelial tumors of the pancreas. Pathologe **18**: 233-237, 1997.
14. Movahedi-Lankarani S, Hruban RH, Westra WH, et al. Primitive neuroectodermal tumors of the pancreas; a report of seven cases of a rare neoplasm. Am J Surg Pathol **26**: 1040-1047, 2002.
15. Perek S, Perek A, Sarman K, et al. Primitive neuroectodermal tumor of the pancreas. A case report of an extremely rare tumor. Pancreatology **2**: 352-356, 2003.
16. Welsch T, Mechtersheimer G, Aulmann S, et al. Huge primitive neuroectodermal tumor of the pancreas: report of a case and review of the literature. World J Gastroenterol **12**: 6070-6073, 2006.
17. Takeuchi M, Kuwae Y, Hamana K, et al. Primitive neuroectodermal tumor of the pancreas. Arch Histopathol D D **10**: 23-26, 2003.
18. Paulussen M, Ahrens S, Dunst J, et al. Localized Ewing tumor of bone: final results of the cooperative Ewing's Sarcoma Study CESS 86. J Clin Oncol **19**: 1818-1829, 2001.
19. Schuck A, Ahrens S, Paulussen M, et al. Local therapy in localized Ewing tumors: results of 1058 patients treated in the CESS 81, CESS 86, and EICESS 92 trials. Int J Radiat Oncol Biol Phys **55**: 1668-177, 2003.

Biomaterials 31 (2010) 4139–4145

Contents lists available at ScienceDirect

Biomaterials

journal homepage: www.elsevier.com/locate/biomaterials

Development of a bifunctional immunoliposome system for combined drug delivery and imaging *in vivo*

Bin Feng [a,d], Kazuhito Tomizawa [b,*], Hiroyuki Michiue [a], Xiao-Jian Han [a], Shin-ichi Miyatake [c], Hideki Matsui [a]

[a] *Department of Physiology, Okayama University Graduate School of Medicine, Dentistry and Pharmaceutical Sciences, 2-5-1 Shikata-cho, Okayama 700-8558, Japan*
[b] *Department of Molecular Physiology, Faculty of Medical and Pharmaceutical Sciences, Kumamoto University, Kumamoto 860-8558, Japan*
[c] *Department of Neurosurgery, Osaka Medical College, 2-7 Daigaku-machi, Takatsuki Osaka 569-8686, Japan*
[d] *Department of Biotechnology, Dalian Medical University, Dalian 116044, China*

ARTICLE INFO

Article history:
Received 16 October 2009
Accepted 15 January 2010
Available online 10 February 2010

Keywords:
Glioma cells
EGFR
Immunoliposome
Gaussia luciferase
Bioluminescence
Boron neutron capture therapy

ABSTRACT

The diverse characteristics of immunoliposomes provide advantages for utilization in drug delivery systems. In this study, we fused the antibody affinity motif of protein A (ZZ) with *Gaussia* luciferase (GLase). The fused protein conjugated with an anti-epidermal growth factor receptor (EGFR) monoclonal antibody (GLase-ZZ-His-mAb) was effectively delivered into glioma cells expressing an activated EGFR mutant (EGFRvIII) and the bioluminescence was visualized in the cells. Immunoliposomes were further constructed with DSPE-PEG-MAL for covalent GLase-ZZ-His-mAb conjugation. A fluorescence dye (HPTS) encapsulated in immunoliposomes conjugated with GLase-ZZ-His-mAb was effectively delivered into EGFRvIII-expressing glioma cells. In a murine xenograft model of glioma, moreover, specific targeting of the immunoliposomes was visualized in the tumor. This new bifunctional immunoliposome system has the potential for drug delivery and imaging *in vivo*.

1. Introduction

Liposomes, comprised of naturally-occurring non-cytotoxic phospholipids and cholesterols, have been recognized as a potential drug delivery vehicle for three decades [1]. Their ability to encapsulate water-soluble compounds as well as non-toxic nature surpasses that of all other nanomaterial-based drug delivery platforms [2]. Also, by altering lipid composition, size and surface chemistry, liposomes can be developed into multifunctional constructs to meet the tunable requirements of different DDSs, such as combining diagnostic and therapeutic capabilities, thus providing a universal platform that can simultaneously detect, image and target diseased cells [2].

In recent years, targeted liposomes have emerged as viable candidates for tumor imaging and therapy [3,4]. Tumor-targeting ligands, such as antibodies, or receptor ligands such as folate [5], transferrin [6] and epidermal growth factor (EGF) [7], have been used for targeted ^{10}B delivery in boron neutron capture therapy (BNCT). Targeted liposomes provide an advantage over untargeted liposomes not only because of increased localization to tumor sites but also because of increased interaction with the target cell population once at the tumor sites [8]. Immunoliposomes have also been used to deliver contrast agents and radionuclides for diagnostic imaging and therapy [9–12]. Semiconductor quantum dots (QDs) conjugated to liposomes are used for imaging, and the immunoliposomes are successfully observed *in vitro* and *in vivo* [13].

For real-time imaging in small animals, the bioluminescence produced by the enzymatic reaction of a luciferase with a luciferin has been used to non-invasively monitor biological processes [14]. The methods based on a luciferase–luciferin reaction have been applied to the imaging of tumors in mice with firefly luciferase [15], *Renilla* luciferase [16], and *Vargula* luciferase [17]. As a coelenterazine-dependent luciferase, *Gaussia* luciferase (GLase) was cloned from a marine copepod *Gaussia princes* and has recently been validated as a reporter gene for *in vivo* imaging applications [18,19]. Its small size (19.9 kDa) and independence of ATP make it suitable for detecting bioluminescence when fused with another protein [20–22].

We previously used the antibody affinity motif of protein A (ZZ) as an adaptor to conjugate anti-EGFR antibodies to sodium borocaptate (BSH)-encapsulated nickel-liposomes. The formed immunoliposomes effectively and specifically delivered BSH into EGFR-overexpressing glioma cells *in vitro* and *in vivo* [23]. In the

* Corresponding author. Tel.: +81 96 373 5050; fax: +81 96 373 5052.
E-mail address: tomikt@kumamoto-u.ac.jp (K. Tomizawa).

0142-9612/$ – see front matter © 2010 Elsevier Ltd. All rights reserved.
doi:10.1016/j.biomaterials.2010.01.086

present study, ZZ fused with GLase was used not only as an adaptor to conjugate mAb, but also as an imaging component for detection. Two glioma cell lines, PA U87 not expressing EGFR, and U87 ΔEGFR-overexpressing human EGFR variant III (vIII), were employed to evaluate the efficiency with which the fluorescence dye was delivered and imaging was achieved using the immunoliposomes *in vitro* and *in vivo*.

2. Materials and methods

2.1. Lipids and chemicals

DSPE-PEG-MAL (maleimide), DSPE-PEG_{2000}, DOPC and DOPG were purchased from Nippon Oil and Fats (Tokyo, Japan). Cholesterol, chloroform and diethyl ether were acquired from Wako Pure Chemicals (Japan). 8-Hydroxypyrene-1,3,6-trisulfonic acid trisodium salt (HPTS) and Traut's Reagent (2-Iminothiolane.HCl) were purchased from Sigma–Aldrich and Coelenterazine was purchased from NanoLight Technology.

2.2. Cell lines

U87 ΔEGFR and PA U87 glioma cell lines (kindly donated by Professor Webster K. Cavenee of the University of California at San Diego) were used in all experiments. U87 ΔEGFR cells stably express the constitutively active EGFR, EGFRvIII, whereas PA U87 cells express no EGFR. The cells were maintained in Dulbecco's modified Eagle's medium (DMEM) (Invitrogen) with 10% fetal bovine serum (FBS), penicillin and streptomycin at 37 °C in a humidified atmosphere containing 5% CO_2.

2.3. Expression and purification of recombinant GLase-ZZ-His

The pGLuc plasmid was purchased from LUX biotechnology Ltd (Scotland, UK).The GLase gene was amplified from the plasmid using a sense primer (5′-GAGCTCCATGAAACCAACTGAAAACAATG-3′, underline indicates *Sac*I site) and antisense primer (5′-AAGCTTATCACCACCGGCACCCTT-3′, underline indicates *Hind*III site). The PCR product was ligated into the pCR2.1 TOPO vector (Invitrogen), and digested with *Sac*I and *Hind*III. The digested GLase fragment was then inserted between the *Sac*I-*Hind*III site in the ZZ-His expression plasmid [23]. The recombinant plasmid was transformed into *E. coli* BL21 (DE3). The expression and purification of GLase-ZZ-His were performed as described previously [24].

2.4. Conjugation of GLase-ZZ-His with anti-EGFR antibody or FITC

To conjugate GLase-ZZ-His with the anti-EGFR mouse antibody (101-7300-0, Katayama Chemical Inc., Japan), the two were mixed at a molar ratio of 100:1 (GLase-ZZ-His to antibody) in 200 μL of PBS (pH7.4) and rotated at 4 °C for 2 h to yield GLase-ZZ-His-mAb.

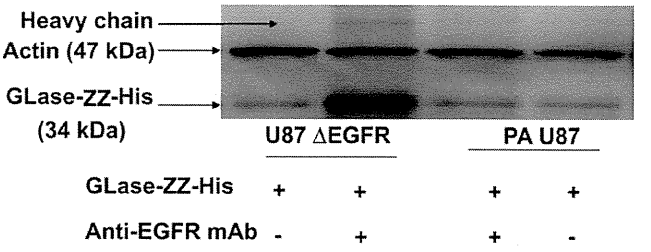

Fig. 1. Antibody-mediated delivery of GLase-ZZ-His into EGFR-overexpressing glioma cells. GLase-ZZ-His-mAb and GLase-ZZ-His were incubated with U87 ΔEGFR and PA U87 for 2 h. After a wash with PBS, cell lysate was subjected to 10% SDS-PAGE and transferred to PVDF membranes. The delivered proteins were detected by Western blotting using anti-His mouse mAb.

For the preparation of FITC-GLase-ZZ-His, GLase-ZZ-His was incubated with 1 mg/mL of fluorescein isothiocyanate isomer I (FITC, Sigma–Aldrich) at room temperature for 15 min with further incubation at 4 °C overnight in PBS as described [25]. The molar ratio of FITC to GLase-ZZ-His was 2:1. After incubation, non-reacted FITC was removed using a PD-10 column (Amersham). To conjugate FITC-GLase-ZZ-His with the anti-EGFR mouse antibody (FITC-GLase-ZZ-His-mAb), the two were mixed at the molar ratio mentioned above.

2.5. Confirmation of the delivery of GLase-ZZ-His-mAb and FITC-GLase-ZZ-His-mAb in cells

PA U87 and U87 ΔEGFR cells were incubated with 3 μM of GLase-ZZ-His-mAb. As a control, the cells were incubated with 3 μM of GLase-ZZ-His. After 2 h, the cells were washed with PBS twice and treated with 0.025% trypsin to remove surface-bound antibody. They were then resuspended in PBS twice before sonication and subjected to Western blotting using an anti-His mouse monoclonal antibody (C-term, Invitrogen). The Western blotting was carried out as described previously [26]. After incubation with the appropriate secondary antibody conjugated with horseradish peroxidase (Sigma–Aldrich), positive bands were visualized using an enhanced chemiluminescence detection system (Amersham Biosciences, Pittsburgh, PA).

After 3 h of incubation with FITC-GLase-ZZ-His-mAb, U87 ΔEGFR and PA U87 cells were washed with PBS twice, then fixed with 4% paraformaldehyde (PFA) for 10 min, and washed with PBS three more times. Fluorescence was observed using

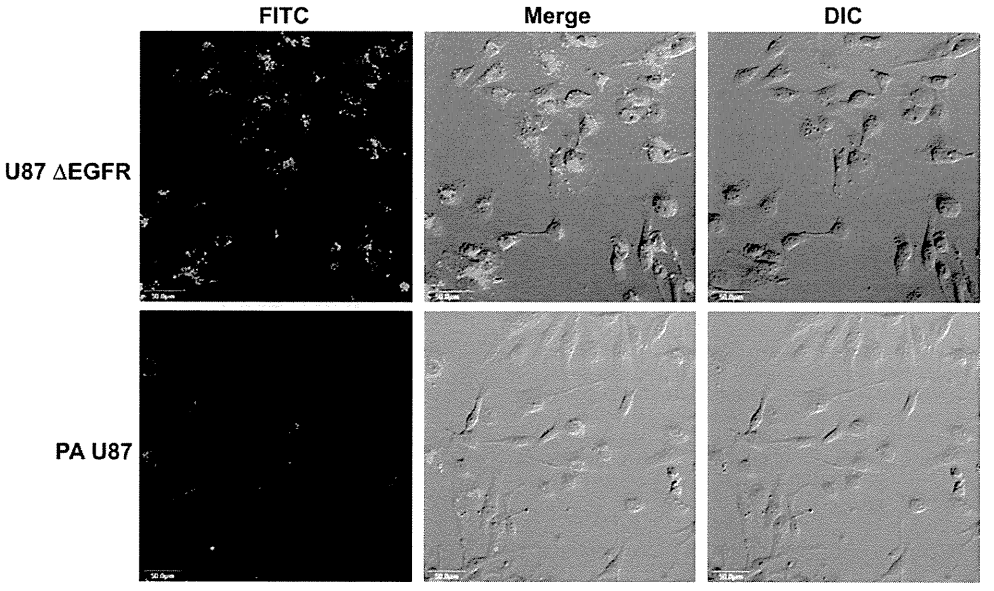

Fig. 2. Fluorescence-based detection of GLase-ZZ-His delivered by the antibody. U87 ΔEGFR and PA U87 cells were incubated with FITC-GLase-ZZ-His-mAb for 2 h and fixed with 4% PFA. Fluorescence was visualized using a confocal laser microscope. Bar = 50 μm.

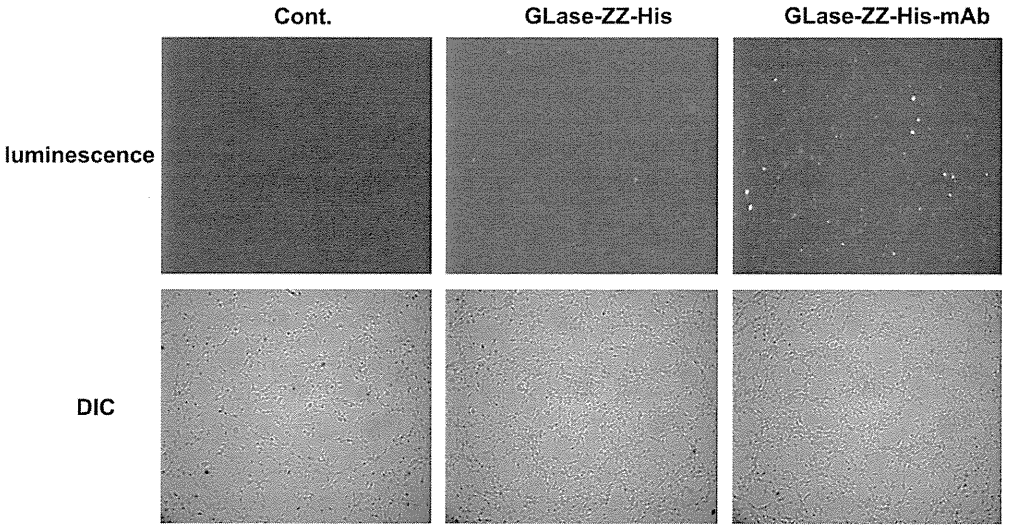

Fig. 3. Bioluminescence-based detection of GLase-ZZ-His in U87 ΔEGFR cells. U87 ΔEGFR cells were incubated with GLase-ZZ-His and GLase-ZZ-His-mAb for 2 h. After being washed with culture medium without serum, the cells were treated with coelenterazine and immediately observed under a bioluminescence microscope.

a confocal laser microscope (FluoView, Olympus, Japan). In the control, only FITC-GLase-ZZ-His was added.

2.6. Bioluminescence imaging of GLase-ZZ-His in cells

To detect the bioluminescence of GLase-ZZ-His, U87 ΔEGFR cells were cultured on a 35-mm glass-bottomed dish for 24–48 h. GLase-ZZ-His-mAb and GLase-ZZ-His were added at 3 μM and the cells were incubated for 2 h, washed with DMEM two times, and soaked with 1 mL of serum-free DMEM containing 1 μg/mL of coelenterazine. Luminescence was immediately recorded with an Olympus Luminoview LV 200 (Bioluminescence microscope (BLM)) after the addition of coelenterazine. Images were acquired and analyzed with Metamorph software (Molecular devices).

2.7. Construction of GLase-ZZ-His-immunoliposomes

Liposomes composed of DOPC: DOPG: CH: DSPE-PEG-MAL: DSPE-PEG_{2000} (3:3:4:0.1:0.1, molar ratio) were prepared by lipid film hydration as described previously with a slight modification [27]. Briefly, 100 μmol of lipid dissolved in 2 mL of a chloroform/diethyl ether mixture (1:1 v/v) was added to a rotary evaporator to form a lipid film under reduced pressure. Two milliliters of PBS containing 35 mM HPTS was then added and the lipid film was vortexed. To control size and lamellarity, the suspension was sonicated by a tip-type ultrasonic homogenizer (output level 7, TAITEC ULTRS Homogenizer VP-5S, Tokyo, Japan) for 5 × 1 min with 1 min ice cooling interval between each round. Then the liposome emulsion was extruded 10 times through a polycarbonate membrane 100 nm in pore size using an extruder device at 50 °C. The mean diameter of the prepared liposomes was determined with an electrophoretic light scattering spectrophotometer (ELS-8000, Photal, Tokyo, Japan). Unencapsulated free HPTS was removed by a PD-10 desalting column (Amersham).

For protein thiolation, GLase-ZZ-His was incubated with Traut's reagent at a molar ratio of 1:2 in PBS (pH7.4) with 0.5 M EDTA. After incubation at room temperature for 1 h, the thiolated GLase-ZZ-His was separated using a PD-10 column, and the fractions containing thiolated GLase-ZZ-His were pooled. Under a nitrogen atmosphere, HPTS-loaded liposomes containing DSPE-PEG_{2000}-maleimide were incubated with thiolated GLase-ZZ-His (molar ratio of DSPE-PEG_{2000}-maleimide to GLase-ZZ-His, 40:1) overnight at room temperature at a low rotating speed [28]. Free GLase-ZZ-His was removed with a Sepharose CL-4B column (1 × 10 cm) and the eluted GLase-ZZ-His-liposomes (Hereafter abbreviate as pre-immunoliposomes) were concentrated and the protein concentration was measured with a Biadford protein assay (Bio-rad). For constructing the immunoliposomes conjugated with anti-EGFR mouse antibody (mAb), the antibody was mixed with pre-immunoliposomes at a molar ratio of 1:20 (mAb to GLase-ZZ-His) at 4 °C with rotation for 2 h. Free mAbs were removed with a Sepharose CL-4B column. The lipid in each fraction was analyzed by the DAOS method using a Phospholipids C reagent kit (Wako Pure Chemical Inc. Ltd., Japan)

2.8. Fluorescence signal and luciferase detection in immunoliposome-treated cells

U87 ΔEGFR cells were cultured on laminin (20 μg/mL)-coated 3 cm dishes (2 mL medium) for 24–48 h, after which immunoliposomes and pre-immunoliposomes were added. The final concentrations of liposome (total lipid), GLase-ZZ-His, and antibody were 1 mM, 2 μM, and 3 μg/mL, respectively. After 2 h incubation, the cells were washed with DMEM twice, fixed with 4% PFA for 10 min, and washed with PBS twice again. Fluorescence signals were observed using a confocal laser microscope. For the detection of GLase-ZZ-His in immunoliposome-treated cells, U87 ΔEGFR cells were washed with DMEM and bioluminescence signals were analyzed as mentioned in 2.6.

2.9. Bioluminescence imaging in vivo

U87 ΔEGFR cells (1×10^6 cells/100 μL) were implanted into the back of female 4-to-6 week-old nude mice (15–20 g, BALB/c Slc-nu/nu; Japan SLC). After 10–14 days, animals bearing palpable tumors were administered intravenously 400 μL of immunoliposomes and pre-immunoliposomes via the tail. After 4 h, mice were imaged by injecting 50 μL of coelenterazine solution (100 μg/mL) at the tumor site under anesthesia using a cooled CCD (IVIS, Xenogen, Alameda, CA) camera as described previously [22]. The intensity of the selected region over the tumor was recorded as maximum photons s^{-1} cm^{-2} $steradian^{-1}$. To obtain control signal intensity, same amount of coelenterazine was injected to the site without tumor.

2.10. Slice analysis for determining HPTS's distribution in tumor

The immunoliposome-injected mice were sacrificed soon after bioluminescence imaging and tissues containing the tumor were excised. Sections 10-μm thick were

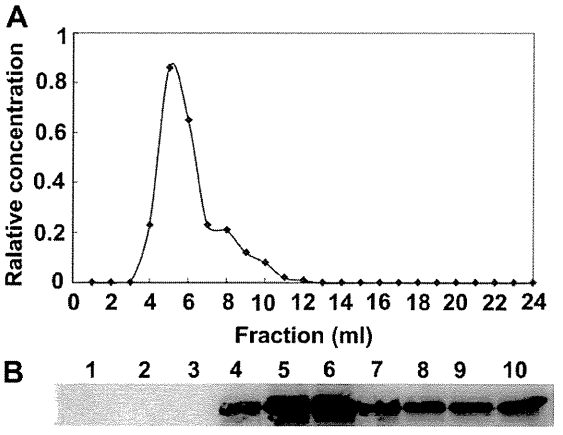

Fig. 4. Characterization of GLase-ZZ-His conjugated to liposomes. (A) GLase-ZZ-His-immunoliposomes (pre-immunoliposomes) were eluted through a Sepharose column and detected by lipid analysis. (B) Ten-microliter aliquots of eluted pre-immunoliposome samples were subjected to 10% SDS-PAGE and transferred to PVDF membranes. Anti-His mouse monoclonal antibody was used for the detection of GLase-ZZ-His.

cut on a microtome (CM 1850, Leica Microsystems, Wetzlar, Germany) and the fluorescence signal of HPTS was observed immediately using a confocal laser microscope (FluoView, Olympus, Japan).

3. Results

3.1. Delivery of GLase-ZZ-His-mAb into U87 ΔEGFR cells

Little of GLase-ZZ-His was delivered into U87 ΔEGFR cells overexpressing the constitutively active EGFR mutant, EGFRvIII (Fig. 1). When conjugated with the anti-EGFR mouse antibody (GLase-ZZ-His-mAb), however, GLase-ZZ-His was effectively delivered (Fig. 1). In PA U87 cells, which had no EGFR expression, the GLase-ZZ-His level was low even when GLase-ZZ-His was conjugated with the mAb (Fig. 1).

GLase-ZZ-His-mAb was next labelled with FITC and its delivery into U87 ΔEGFR and PA U87 cells was examined using a confocal microscope (Fig. 2). GLase-ZZ-His-mAb was observed in almost all U87 ΔEGFR cells (Fig. 2). A Z-dimensional scan excluded the possibility that the GLase-ZZ-His was attached to the cell surface (Supplementary material). In contrast, weak fluorescence was detected in PA U87 cells (Fig. 2). The results were consistent with those of Western blotting in Fig. 1, and suggest that GLase-ZZ-His was targeted and delivered into the EGFRvIII-overexpressing cells when conjugated with the anti-EGFR antibody.

3.2. Bioluminescence activity of GLase-ZZ-His-mAb in U87 ΔEGFR cells

To clarify whether GLase-ZZ-His had bioluminescence in glioma cells, GLase-ZZ-His was conjugated with the anti-EGFR mAb and added to the culture medium of U87 ΔEGFR cells. A strong signal was detected in the cells (Fig. 3). In GLase-ZZ-His incubated cells, in

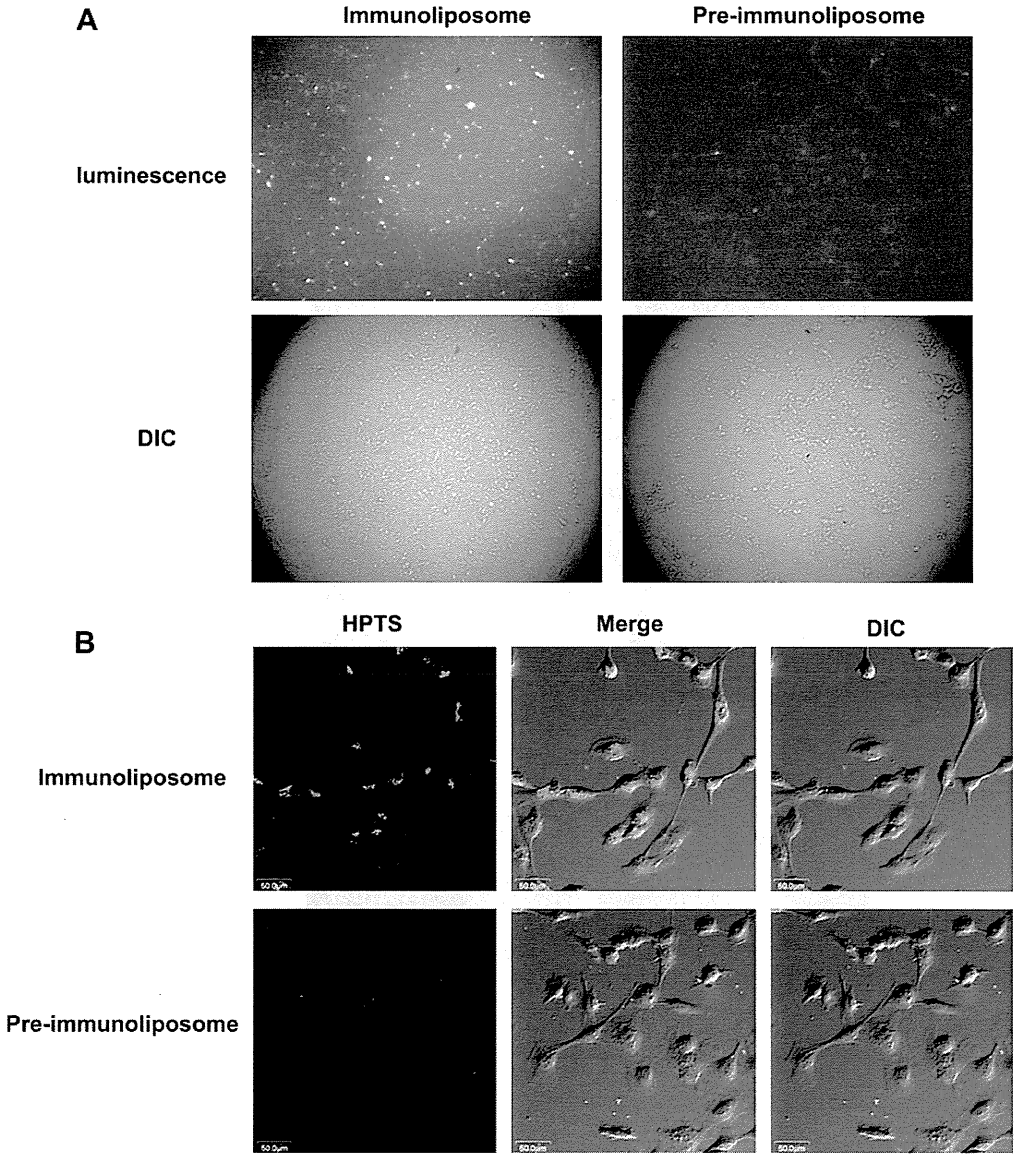

Fig. 5. Bioluminescence and fluorescence-based detection of immunoliposomes delivered into glioma cells. (A) U87 ΔEGFR cells were incubated with immunoliposomes and pre-immunoliposomes for 2 h. After a washing with DMEM, the luminescence was recorded soon after the coelenterazine substrate was added to cells. (B) After the luminescence was observed, the same samples were observed under a confocal microscope to detect fluorescence. Bar = 50 μm.

contrast, weak bioluminescence was detected in a few cells (Fig. 3). The bioluminescence was underdetectable in intact cells (Cont.). These results suggest that the fusion of ZZ-His with GLase did not affect its luciferase function.

3.3. Confirmation of the conjugation of GLase-ZZ-His with pre-immunoliposomes

To investigate whether thiolated GLase-ZZ-His effectively reacted with the maleimide (MAL) group on the liposome's surface, we compared the position of the GLase-ZZ-His and pre-immunoliposome after their separation with Sepharose CL-4B. The peak of the pre-immunoliposome occurred between fractions 5 and 6 (Fig. 4A). Western blotting revealed that GLase-ZZ-His was also abundant in these fractions (Fig. 4B). The results showed that thiolated GLase-ZZ-His was conjugated to the liposome's surface through the MAL-SH group via a covalent reaction. The immunoliposome was eventually produced through conjugation of the anti-EGFR antibody with the pre-immunoliposome.

3.4. Immunoliposome-mediated delivery of HPTS and imaging of GLase-ZZ-His in U87 ΔEGFR cells

To investigate whether immunoliposomes conjugated with the anti-EGFR antibody targeted U87 ΔEGFR cells and are useful for the delivery of chemicals and the imaging of tumors, HPTS, a fluorescence chemical, was encapsulated in the immunoliposome and U87 ΔEGFR cells were incubated with the HPTS-encapsulated immunoliposomes. Strong bioluminescence was detected in the cells (Fig. 5A). In contrast, pre-immunoliposomes not conjugated to the mAb, emitted a faint signal in the cells (Fig. 5A). Moreover, the cells were subjected to fluorescence microscopy. The fluorescence from HPTS was strong in the immunoliposome-treated cells but weak in the pre-immunoliposome-treated cells (Fig. 5B).

3.5. In vivo imaging of xenografted brain tumor using immunoliposomes conjugated with anti-EGFR antibody

We investigated whether the immunoliposomes conjugated with the anti-EGFR antibody could be used to image xenografted brain tumor and carry chemicals. Immunoliposomes and pre-immunoliposomes were injected into the tail of tumor-bearing mice. After 4 h, the tumor was imaged by injection with 50 μL of coelenterazine solution (100 μg/mL) at the tumor site. A strong and clear bioluminescence signal was detected at the tumor site (Fig. 6A, left panel) in immunoliposome-treated mice while weak signals were detected at two tumor sites in the pre-immunoliposome-treated mice (Fig. 6A, right panel). As a signal intensity control, much weaker signal was observed at the site without tumor when coelenterazine was injected (data not shown).

To investigate whether HPTS was specifically carried in the tumor, the tumor xenografted regions were sectioned and the

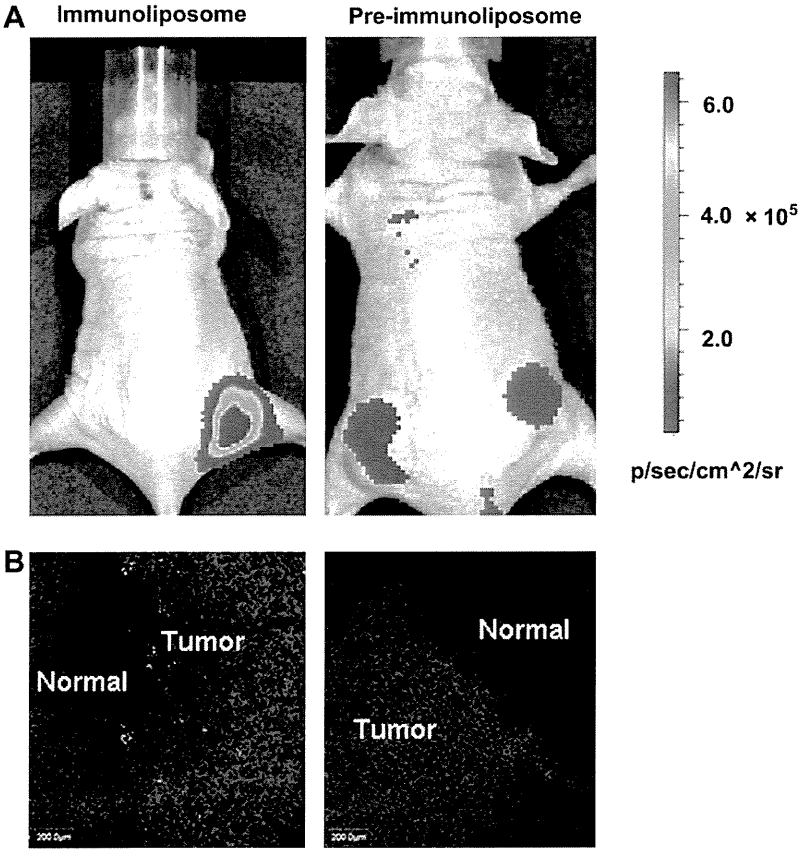

Fig. 6. Bioluminescence imaging in living nude mice harboring U87 ΔEGFR cell xenografts and slice analysis. (A) Images were obtained using a CCD camera 4 h after an intravenous injection of immunoliposomes and pre-immunoliposomes in the tail. A color scale represents p/sec/cm^2/steradian. Left panel, immunoliposome-treated sample. Right panel, pre-immunoliposome-treated sample. (B) A 10-μm section cut from frozen tumor tissue harvested at 4 h post-injection and examined with a confocal microscopy. The tumor section was examined for nuclei stained by Hoechst (blue) and HPTS (green). The blue fluorescence of Hoechst was used to indicate the position of the tumor. Left panel, immunoliposome-treated sample. Right panel, pre-immunoliposome-treated sample. Bar = 200 μm.

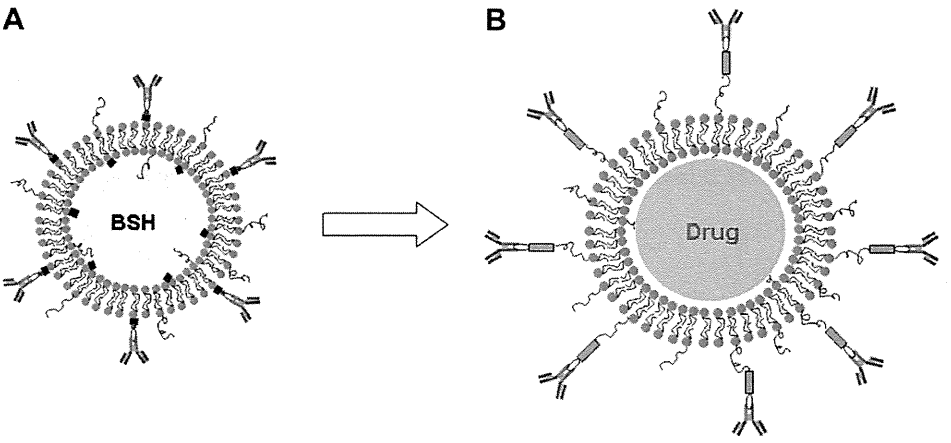

Fig. 7. Development of a bifunctional immunoliposome. (A) Our previous nickel-immunoliposome. (B) The bifunctional immunoliposome.

fluorescence from HPTS was observed using a confocal microscope. The fluorescence was located in the tumor but not in normal tissue in the immunoliposomes-treated mice (Fig. 6B, left panel). In the pre-immunoliposome-treated mice, by contrast, no fluorescence was seen in the tumor or normal regions (Fig. 6B, right panel).

4. Discussion

In the present study, we showed that a fusion protein consisting of ZZ-linked to *Gaussia* luciferase could be used to target and image glioblastoma cells expressing the activated EGFR mutant EGFRvIII. The results support our previous findings obtained with a ZZ conjugated to liposomes for targeting and delivering BSH [23]. Previously, a nickel lipid was used for binding His-tagged ZZ (Fig. 7A) [23]. To avoid possible toxic effects of DOGS-NTA-Ni, we replaced it with DSPE-PEG-MAL for the covalent reaction to conjugate GLase-ZZ-His with the liposome in the present study. Thus, GLase-ZZ-His was located at the distal end of the immunoliposome. The antibody conjugated to ZZ is thought to be located further out than in our previous immunoliposome (Fig. 7B). The design of the new immunoliposome may improve the antibody's ability to recognize and bind tumor cells. Moreover, the usage of an appropriate ratio of DSPE-PEG_{2000} made the immunoliposome more stable. Since the mid-1990s, to increase specific binding while also retaining a long period of circulation, researchers have attached an antibody or ligand to PEG's terminus via a thioether bond [28,29]. This design is used widely by researchers [28,29], but the effect of the thiolation reaction on the stability and affinity of the antibody has not been discussed. In the present study, we followed the same basic design but made some improvements. That is, the antibody was conjugated to PEG via the adaptor GLase-ZZ-His, and remained intact because its Fc part bound with ZZ. The construction of the new immunoliposome prevents shorter circulation times using a complete antibody, due to the rapid identification and uptake of the Fc fragment by macrophages in circulation *in vivo* [30].

In recent years, *Gaussia* luciferase has mostly been used for non-invasive studies because of its high quantum yield compared with firefly luciferase and *Renilla* luciferase [31]. GLase has been used to image cultured cells implanted subcutaneously into nude mice [32]. A recent study showed that GLase fused with an anti-carcinoembryomic antigen (CEA) fragment was capable of targeting and imaging human colon carcinoma cells in nude mice [22]. However, its utilization for detecting the distribution of immunoliposomes has not been reported. In the present study, immunoliposomes conjugated with GLase-ZZ-His and anti-EGFR antibody were used to target and image EGFRvIII-expressing glioma cells both *in vitro* and *in vivo*. Although the luciferase signal was detected at the tumor site by a direct coelenterazine solution injection, the signal intensity is much stronger than those in pre-immunoliposome-treated sample (Fig. 6) and at the site without tumor (data not shown), indicating the GLase on immunoliposome targeted to the tumor site by ZZ conjugated antibody. These results suggest that the bioluminescence of GLase is not affected by thiolation and immunoliposomes conjugated with GLase may be useful for the imaging of tumor cells expressing EGFR. The monitoring of liposomes *in vivo* provides valuable information on drug delivery although the development of this technology is still in its early stages.

The combination of a diagnostic test and a therapeutic entity is termed theranostics [33]. Some chemotherapeutics have been directly or indirectly radiolabeled for single photon emission computed tomography (SPECT) and positron emission tomography (PET) imaging [34]. The radiolabeled chemotherapeutics have been injected into patients for the purpose of better understanding their biodistribution and metabolism and to assess whether there exists a relationship between their uptake in tumor tissue and response to treatment [34]. In the present study, our bifunctional immunoliposomes effectively delivered their cargo to the tumor and also were imaged in nude mice. The present results suggest our bifunctional immunoliposomes to be useful for BNCT as a theranostics reagent.

5. Conclusions

The present study showed the utility of bifunctional immunoliposomes fused with GLase-ZZ-His-mAb for the imaging and targeting of glioma cells both *in vitro* and *in vivo*. A thiolated fusion protein of ZZ (Fc-affinity domain) and GLase was conjugated to the immunoliposomes for antibody binding and imaging. We have demonstrated the utility of *Gaussia princeps* luciferase for detecting the distribution of immunoliposomes. Bioluminescence and fluorescence analyses indicated that GLase-ZZ-His and HPTS were successfully delivered into EGFR-overexpressing glioma cells *in vitro* and *in vivo*. Thus, our bifunctional immunoliposome system provides the potential for drug delivery and imaging in tumors.

Acknowledgements

This work was supported by a Grant-in-aid for Scientific Research from the Ministry of Education, Science, Sports and

Culture of Japan and by a Grant-in-aid for Scientific Research from the Ministry of Health, Labour and Welfare of Japan.

Supplementary data

Supplementary material associated with this paper can be found, in the online version, at doi:10.1016/j.biomaterials.2010.01.086

Appendix

Figures with essential colour discrimination. Certain figures in this article, in particular Figs. 4 and 7, that are difficult to interpret in black and white. The full colour images can be found in the online version, at doi:10.1016/j.biomaterials.2010.01.086

References

[1] Maurer N, Fenske DB, Cullis PR. Developments in liposomal drug delivery systems. Expert Opin Biol Ther 2001;1:923–47.
[2] Jiang W, Kim BY, Rutka JT, Chan WC. Advances and challenges of nanotechnology-based drug delivery systems. Expert Opin Drug Deliv 2007;4:621–33.
[3] Elbayoumi TA, Pabba S, Roby A, Torchilin VP. Antinucleosome antibody-modified liposomes and lipid-core micelles for tumor-targeted delivery of therapeutic and diagnostic agents. J Liposome Res 2007;17:1–14.
[4] Sajja HK, East MP, Mao H, Wang YA, Nie S, Yang L. Development of multifunctional nanoparticles for targeted drug delivery and noninvasive imaging of therapeutic effect. Curr Drug Discov Technol 2009;6:43–51.
[5] Pan XQ, Wang H, Lee RJ. Boron delivery to a murine lung carcinoma using folate receptor-targeted liposomes. Anticancer Res 2002;22:1629–33.
[6] Maruyama K, Ishida O, Kasaoka S, Takizawa T, Utoguchi N, Shinohara A, et al. Intracellular targeting of sodium mercaptoundecahydrododecaborate (BSH) to solid tumors by transferrin-PEG liposomes, for boron neutron-capture therapy (BNCT). J Control Release 2004;98:195–207.
[7] Bohl Kullberg E, Bergstrand N, Carlsson J, Edwards K, Johnsson M, Sjöberg S, et al. Development of EGF-conjugated liposomes for targeted delivery of boronated DNA binding agents. Bioconjug Chem 2002;13:737–43.
[8] Sofou S, Sgouros G. Antibody-targeted liposomes in cancer therapy and imaging. Expert Opin Drug Deliv 2008;5:189–204.
[9] Erdogan S, Roby A, Sawant R, Hurley J, Torchilin VP. Gadolinium-loaded polychelating polymer-containing cancer cell-specific immunoliposomes. J Liposome Res 2006;16:45–55.
[10] Kostarelos K, Emfietzoglou D. Tissue dosimetry of liposome-radionuclide complexes for internal radiotherapy: toward liposome-targeted therapeutic radiopharmaceuticals. Anticancer Res 2000;20:3339–45.
[11] Erdogan S, Medarova ZO, Roby A, Moore A, Torchilin VP. Enhanced tumor MR imaging with gadolinium-loaded polychelating polymer-containing tumor-targeted liposomes. J Magn Reson Imaging 2008;27:574–80.
[12] Torchilin VP. Polymeric contrast agents for medical imaging. Curr Pharm Biotechnol 2000;1:183–215.
[13] Weng KC, Noble CO, Papahadjopoulos-Sternberg B, Chen FF, Drummond DC, Kirpotin DB, et al. Targeted tumor cell internalization and imaging of multifunctional quantum dot-conjugated immunoliposomes *in vitro* and *in vivo*. Nano Lett 2008;8:2851–7.
[14] Welsh DK, Kay SA. Bioluminescence imaging in living organisms. Curr Opin Biotechnol 2005;16:73–8.
[15] Swijnenburg RJ, Schrepfer S, Cao F, Pearl JI, Xie X, Connolly AJ, et al. *In vivo* imaging of embryonic stem cells reveals patterns of survival and immune rejection following transplantation. Stem Cells Dev 2008;17:1023–9.
[16] Bhaumik S, Lewis XZ, Gambhir SS. Optical imaging of Renilla luciferase, synthetic Renilla luciferase, and firefly luciferase reporter gene expression in living mice. J Biomed Opt 2004;9:578–86.
[17] Thompson EM, Adenot P, Tsuji FI, Renard JP. Real time imaging of transcriptional activity in live mouse preimplantation embryos using a secreted luciferase. Proc Natl Acad Sci U S A 1995;92:1317–21.
[18] Verhaegent M, Christopoulos TK. Recombinant *Gaussia* luciferase. Overexpression, purification, and analytical application of a bioluminescent reporter for DNA hybridization. Anal Chem 2002;74:4378–85.
[19] Tannous BA. *Gaussia* luciferase reporter assay for monitoring biological processes in culture and *in vivo*. Nat Protoc 2009;4:582–91.
[20] Suzuki T, Usuda S, Ichinose H, Inouye S. Real bioluminescence imaging of a protein secretory pathway in living mammalian cells using *Gaussia* luciferase. FEBS Lett 2007;581:4551–6.
[21] Venisnik KM, Olafsen T, Loening AM, Iyer M, Gambhir SS, Wu AM. Bifunctional antibody-Renilla luciferase fusion protein for *in vivo* optical detection of tumors. Protein Eng Des Sel 2006;19:453–60.
[22] Venisnik KM, Olafsen T, Gambhir SS, Wu AM. Fusion of *Gaussia* luciferase to an engineered anti-carcinoembryonic antigen (CEA) antibody for *in vivo* optical imaging. Mol Imaging Biol 2007;9:267–77.
[23] Feng B, Tomizawa K, Michiue H, Miyatake S, Han XJ, Fujimura A, et al. Delivery of sodium borocaptate to glioma cells using immunoliposome conjugated with anti-EGFR antibodies by ZZ-His. Biomaterials 2009;30:1746–55.
[24] Feng B, Zhao CH, Tanaka S, Imanaka H, Imamura K, Nakanishi K. TPR domain of Ser/Thr phosphatase of *Aspergillus oryzae* shows no autoinhibitory effect on the dephosphorylation activity. Int J Biol Macromol 2007;41:281–5.
[25] Hashizume T, Fukuda T, Nagaoka T, Tada H, Yamada H, Watanabe K, et al. Cell type dependent endocytic internalization of ErbB2 with an artificial peptide ligand that binds to ErbB2. Cell Biol Int 2008;32:814–26.
[26] Tomizawa K, Iga N, Lu YF, Moriwaki A, Matsushita M, Li ST, et al. Oxytocin improves long-lasting spatial memory during motherhood through MAP kinase cascade. Nat Neurosci 2003;6:384–90.
[27] Kheirolomoom A, Ferrara KW. Cholesterol transport from liposomal delivery vehicles. Biomaterials 2007;28:4311–20.
[28] Béduneau A, Saulnier P, Hindré F, Clavreul A, Leroux JC, Benoit JP. Design of targeted lipid nanocapsules by conjugation of whole antibodies and antibody Fab' fragments. Biomaterials 2007;28:4978–90.
[29] Kirpotin D, Park JW, Hong K, Zalipsky S, Li WL, Carter P, et al. Sterically stabilized anti-HER2 immunoliposomes: design and targeting to human breast cancer cells in vitro. Biochemistry 1997;36:66–75.
[30] Kamps JA, Scherphof GL. Receptor versus non-receptor mediated clearance of liposome. Adv Drug Deliv Rev 1998;32:81–97.
[31] Tannous BA, Kim DE, Fernandez JL, Weissleder R, Breakefield XO. Codon-optimized *Gaussia* luciferase cDNA for mammalian gene expression in culture and *in vivo*. Mol Ther 2005;11:435–43.
[32] Wurdinger T, Badr C, Pike L, de Kleine R, Weissleder R, Breakefield XO, et al. A secreted luciferase for *ex vivo* monitoring of *in vivo* processes. Nat Methods 2008;5:171–3.
[33] Del Vecchio S, Zannetti A, Fonti R, Pace L, Salvatore M. Nuclear imaging in cancer theranostics. Q J Nucl Med Mol Imaging 2007;51:152–63.
[34] Rottey S, Signore A, Van de Wiele C. Radiolabelled chemotherapeutics. Q J Nucl Med Mol Imaging 2007;51:139–51.

悪性脳腫瘍に対する最新放射線治療とその成績
—放射線治療における外科治療の役割—

宮 武 伸 一

脳神経外科ジャーナル別刷 VOL. 19 NO. 12 2010年12月